1 **TRIM7 ubiquitinates SARS-CoV-2 membrane protein to limit apoptosis and viral**
2 **replication**
3
4 Maria Gonzalez-Orozco[1], Hsiang-chi Tseng[2], Adam Hage[1], Hongjie Xia[3], Padmanava
5 Behera[2], Kazi Afreen[2], Yoatzin Peñaflor-Tellez[2], Maria I. Giraldo[1], Matthew Huante[1],
6 Lucinda Puebla-Clark[4], Sarah van Tol[1], Abby Odle[2], Matthew Crown[5], Natalia Teruel[6],
7 Thomas R Shelite[4], Vineet Menachery[1], Mark Endsley[1], Janice J. Endsley[1], Rafael J.
8 Najmanovich[6], Matthew Bashton[5], Robin Stephens[4,7], Pei-Yong Shi[3], Xuping Xie[3],
9 Alexander N. Freiberg[8], Ricardo Rajsbaum[1,2,*]
10
11 **Author affiliations and footnotes**
12
13 [1]Department of Microbiology and Immunology, University of Texas Medical Branch,
14 Galveston, TX
15 [2]Center for Virus-Host-Innate-Immunity, RBHS Institute for Infectious and Inflammatory
16 Diseases, and Department of Medicine, New Jersey Medical School, Rutgers
17 University, Newark, NJ
18 [3]Department of Biochemistry and Molecular Biology, University of Texas Medical
19 Branch, Galveston, TX
20 [4]Department of Internal Medicine, Division of Infectious Diseases, University of Texas
21 Medical Branch, Galveston, TX
22 [5]Hub for Biotechnology in the Built Environment, Department of Applied Sciences,
23 Faculty of Health and Life Sciences, Northumbria University, Newcastle, UK
24 [6]Department of Pharmacology and Physiology, Faculty of Medicine, Université de
25 Montréal, Montreal, Canada
26 [7]Center for Immunity and Inflammation and Department of Pharmacology, Physiology
27 and Neuroscience, New Jersey Medical School, Rutgers University, Newark, NJ
28 [8]Department of Pathology, University of Texas Medical Branch, Galveston, TX
29 [*]Corresponding author: ricardo.rajsbaum@rutgers.edu
30
31
32
33
34
35
36
37
38
39
40
41
42
43
44
45
46

Abstract

SARS-CoV-2 is a highly transmissible virus that causes COVID-19 disease. Mechanisms of viral pathogenesis include excessive inflammation and viral-induced cell death, resulting in tissue damage. We identified the host E3-ubiquitin ligase TRIM7 as an inhibitor of apoptosis and SARS-CoV-2 replication via ubiquitination of the viral membrane (M) protein. *Trim7*$^{-/-}$ mice exhibited increased pathology and virus titers associated with epithelial apoptosis and dysregulated immune responses. Mechanistically, TRIM7 ubiquitinates M on K14, which protects cells from cell death. Longitudinal SARS-CoV-2 sequence analysis from infected patients revealed that mutations on M-K14 appeared in circulating variants during the pandemic. The relevance of these mutations was tested in a mouse model. A recombinant M-K14/K15R virus showed reduced viral replication, consistent with the role of K15 in virus assembly, and increased levels of apoptosis associated with the loss of ubiquitination on K14. TRIM7 antiviral activity requires caspase-6 inhibition, linking apoptosis with viral replication and pathology.

Keywords: SARS-CoV-2, Membrane protein, E3-Ubiquitin ligases, TRIM7, Ubiquitination, Apoptosis, Antiviral activity, Caspase-6.

INTRODUCTION

The severe acute respiratory syndrome coronavirus 2 (SARS-CoV-2) is a highly transmissible positive single-stranded RNA virus of the *Coronaviridae* family [1,2]. Its RNA genome encodes four structural proteins, which include Spike (S), Nucleocapsid (N), Envelope (E), and Membrane (M) proteins [3]. Of the structural proteins, M is the most abundant in the virion and is essential for the sorting of structural proteins to promote assembly and release of viral particles [4].

The pathogenesis of SARS-CoV-2 in humans includes a combination of excessive inflammatory responses and viral-induced tissue damage that causes lung injury, called acute respiratory distress syndrome [5] [2,6,7]. The severity of disease and respiratory failure in human-infected patients correlates with the increased presence of cytokines including IL-1-β, IL-6, and TNF-α in serum and BAL [8,9]. SARS-CoV-2 infects multiciliated cells of the respiratory tract and alveolar type 2 (AT2) cells expressing the ACE2 receptor and the TMPRSS2 protease [5,10-12]. Viral infection can increase levels of apoptosis and other forms of cell death leading to tissue damage. Together, increased cell death and enhanced inflammation can correlate with disease [12-14]. Multiple mechanisms have been proposed to promote cell death during infection, including cytokine-induced or intrinsic apoptosis directly triggered by viral proteins, including M [15,16]. The M protein can also promote apoptosis by inhibiting the activation of the PDK1-AKT pathway [17], or by inducing mitochondrial intrinsic apoptosis [18].

The innate immune response elicited by SARS-CoV-2 infection includes innate lymphoid cells, monocytes, macrophages, and neutrophils [19,20]. In COVID-19 patients, low levels of circulating lymphocytes and increased levels of neutrophils correlate with the severity of the infection [21,22]. However, neutrophils are not the main cell type found in the lungs of human patients with prolonged severe disease, and there is evidence suggesting that neutrophils may be protective early during infection [19]. It is still unclear which specific factors during SARS-CoV-2 infection contribute to this shift from protective to detrimental responses by neutrophils and monocytes. Similarly, type-I interferons (IFN-I), which are well-known antiviral cytokines, can play protective or detrimental roles during infection depending on timing [23,24], however, it is also unclear what factors determine protective IFN-I induction.

The innate antiviral response against SARS-CoV-2 is mediated primarily by the cytosolic nucleic acid sensor melanoma differentiation-associated protein 5 (MDA5) that recognizes the viral RNA to activate the mitochondrial antiviral signaling protein (MAVS) leading to the production of IFNs and proinflammatory cytokines [25,26]. Multiple viral proteins, including M, can inhibit the IFN-I pathway by targeting cytosolic receptors or by promoting the degradation of the TANK-binding kinase (TBK-1), reducing IRF3 phosphorylation and IFN-I induction [27-33].

TRIM7 belongs to a large family of E3-Ubiquitin (Ub) ligases, which transfer Ub to target proteins [34] and can play protective or detrimental roles during infection. TRIM7 has been reported to play antiviral roles against Enteroviruses [35,36], and proviral roles during Zika virus infection (ZIKV) [37]. TRIM7 can also regulate immune responses by promoting the production of IFN-β, TNF-α, and IL-6 in macrophages after TLR4 stimulation [38]. Although there is previous evidence that TRIM7 may interact with M [39] and previous reports identified another E3-ligase, RNF5, as a proviral factor by ubiquitinating M on

139 K15 [40], the pathophysiological roles of TRIM7 and ubiquitination of M *in vivo* during
140 SARS-CoV-2 infection remains unknown. Here we characterized in detail the multiple
141 roles of TRIM7 during infection *in vivo*. We found that TRIM7 regulates the expression
142 of inflammatory cytokines, including the chemokine CXCL1, which promotes the
143 recruitment of immune cells to the infection site. TRIM7 also acts as an antiviral factor
144 during SARS-CoV-2 infection, by ubiquitinating the M protein and inhibiting caspase-6-
145 dependent apoptosis, in an IFN-I independent manner. We also identified the presence
146 of natural K14 mutations in circulating SARS-CoV-2 during the pandemic, supporting a
147 physiological role for ubiquitination of M.
148
149
150 **RESULTS**
151
152 **TRIM7 Ubiquitinates SARS-CoV-2 M protein on the K14 residue**
153 Previous mass spectrometry studies identified TRIM7 as a potential binding partner of
154 SARS-CoV-2 M protein [39], although this interaction and its functional relevance were not
155 further investigated. We first confirmed that TRIM7 and M interact using co-
156 immunoprecipitation assays (coIP) (Fig.1a-b), and this interaction is mediated by
157 TRIM7's PRY-SPRY C-terminal domain (Fig. S1a). As previously proposed [39,40], a
158 significant proportion of M is ubiquitinated when ectopically expressed (Fig. S1b). In
159 addition, overexpression of TRIM7 further enhanced the ubiquitination of M (Fig. 1b-c),
160 whereas a catalytically inactive mutant lacking the RING domain of TRIM7 did not (Fig.
161 1c). Ectopic expression of the ovarian tumor deubiquitinase (OTU), which cleaves
162 endogenous polyubiquitin chains (polyUb) from modified proteins [37], removed all polyUb
163 that coimmunoprecipitated with M, while a catalytically inactive mutant of OTU (OTU-
164 2A) was used as a negative control (Fig. 1c). These results confirm that TRIM7
165 promotes ubiquitination of SARS-CoV-2 M protein.
166 We next asked whether TRIM7 ubiquitinates a specific lysine residue on M. A
167 denaturing pulldown of ectopically expressed His-tagged Ub and M encoding K-to-R
168 mutations, showed reduced TRIM7-mediated ubiquitination on an M-K14R mutant as
169 compared to WT-M (Fig. 1d). The K15 residue on M, which is ubiquitinated by the E3-
170 ligase RNF5 [40], did not appear to be an acceptor for ubiquitination by TRIM7. In further
171 support of this, a K14-only mutant of M, in which all its K residues were mutated to R
172 except for K14 (K14O), showed similar ubiquitination levels as compared to WT M or
173 the K15R mutant, in the presence of overexpressed TRIM7 (Fig.1d). Together, these
174 data suggest that TRIM7 specifically ubiquitinates the M protein on the K14 residue.
175 Ubiquitination of M on K15 by RNF5 is necessary to promote the efficient formation of
176 virus-like-particles (VLPs) and virus release [40]. To rule out a functional role for TRIM7 in
177 virus release, we evaluated the efficiency of VLP formation upon transfection of all viral
178 structural proteins in A549 WT or TRIM7 knockout cells (KO), previously generated in
179 our lab [37]. No apparent differences were observed in the amount of VLPs released from
180 WT and TRIM7 KO (Fig. S1c), suggesting that TRIM7 does not affect virus release,
181 which is consistent with previous observations that the M-K14R mutant is still able to
182 form VLPs [40].
183 Finally, upon ectopic expression, TRIM7 re-localized from discrete punctate cytoplasmic
184 bodies to larger vesicle-like compartments where it colocalized with M (Fig. 1e). In

4

185 addition, M localized in the Golgi compartment (Fig. S1d), as in previous reports [41]. The
186 M-K14R mutant still colocalized and coimmunoprecipitated with TRIM7 (Fig. 1e and
187 S1e), indicating that the interaction did not depend on M-K14 ubiquitination.
188 Overall, these data provide evidence that TRIM7 specifically ubiquitinates M on its K14
189 residue, and this ubiquitination does not affect M's function in the assembly and release
190 of viral particles.
191
TRIM7 has antiviral activity during SARS-CoV-2 infection
193 Since TRIM7 has been reported to have both proviral and antiviral roles, we next
194 evaluated the role of TRIM7 during SARS-CoV-2 infection. Overexpression of TRIM7 in
195 HEK293T cells stably expressing human ACE2 (293T-hACE2) significantly reduced
196 SARS-CoV-2 titers (plaque assay) and viral RNA (qPCR) as compared to the inactive
197 TRIM7-ΔRING, or a vector control (Fig. 2a-b).
198 We then tested whether TRIM7 also has antiviral function *in vivo.* WT and *Trim7*^{-/-} mice
199 [37] were infected with a mouse-adapted strain of SARS-CoV-2 (CMA3p20) [42]. *Trim7*^{-/-}
200 mice lost significantly more weight at the acute phase of infection and showed slower
201 recovery than WT controls (mixed males and females, Fig. 2c). *Trim7*^{-/-} male mice
202 exhibited significantly higher lung viral titers (Fig. 2d) and viral RNA at day 2 and 3 p.i.,
203 while we observed smaller differences between females (Fig. S2a-c). The increase in
204 weight loss and viral titers in *Trim7*^{-/-} mice correlated with clinical scores (e.g., ruffled fur
205 and/or hunched posture, Fig. S2d), as well as consolidation of the airway at later time
206 points (Fig. S2e-f). TRIM7 antiviral effects were most likely independent of the IFN-I
207 response because the levels of IFN-β mRNA were trending higher in *Trim7*^{-/-} and
208 correlated with significantly increased levels of ISG54 and CXCL10, which are well-
209 known ISGs (Fig. 2e-g). In further support of this, IFN-I receptor (IFNAR1) blockade
210 resulted in less weight loss without significantly affecting virus titers as compared to
211 isotype control-treated mice (Fig. 2h-i). As expected, anti-IFNAR1 treated mice showed
212 reduced levels of ISGs (Fig. 2j-k). These results are in line with previous reports
213 showing that IFN-I has a pathogenic effect during SARS-CoV-2 infection, by regulating
214 the infiltration of inflammatory cells but not affecting virus levels [23,24].
215 Together, our data indicates that TRIM7 plays an antiviral role in cell culture and *in vivo.*
216 These effects require TRIM7 E3-ubiquitin ligase activity and do not appear to be IFN
217 mediated.
218
TRIM7 is a negative regulator of IFN-I induction during SARS-CoV-2 infection
220 Although our data suggest that IFN-I is not involved in the TRIM7-mediated antiviral
221 response, elevated IFN induction could still affect inflammatory responses leading to
222 disease. Therefore, we determined whether the increased levels of ISGs observed in
223 *Trim7*^{-/-} infected mice are due to a direct effect of TRIM7 in the IFN pathway. TRIM7
224 represses expression of IFN-I because bone-marrow derived dendritic cells (BMDCs)
225 from *Trim7*^{-/-} mice infected with SARS-CoV-2 showed increased levels of IFN-β mRNA
226 as compared to WT BMDCs (Fig. S2g). In contrast, *Trim7*^{-/-} cells expressed lower levels
227 of IL-1β mRNA when compared with WT BMDCs (Fig. S2h). Although SARS-CoV-2
228 does not productively replicate in DCs [43], the presence of similar levels of viral RNA in
229 WT and KO cells indicated that the effects observed are not due to differences in virus
230 infection (Fig. S2i).

231 To further examine how TRIM7 inhibits IFN-I induction, we tested interactions with the
232 pattern recognition receptors (PRRs) RIG-I and MDA5. Results from coIP assays
233 revealed that TRIM7 interacts with both PRRs (Fig. S2j). Since there is evidence that
234 MDA5 is the major cytosolic receptor for SARS-CoV-2 [25,26], we also evaluated if TRIM7
235 can affect MDA5's induction of IFN-β. IFN luciferase reporter assays showed that
236 increased concentrations of TRIM7 reduced the IFN-β promoter activity (Fig. S2k),
237 suggesting that TRIM7 can negatively regulates IFN-β by inhibiting MDA5-mediated
238 signaling.
239
240 **Ubiquitination on M-K14 does not affect IFN-I antagonist function**
241 M has also been shown to inhibit both the IFN-I production as well as the IFN-I signaling
242 pathways [27-30,44]. Therefore, we examined if M ubiquitination can affect IFN antagonism.
243 Ectopic expression of WT M or a mutant lacking all ubiquitination sites (M-KallR)
244 inhibited IRF3 phosphorylation at comparable levels upon stimulation with the dsRNA
245 mimic poly (I:C) (Fig. S2l), suggesting that ubiquitination on M does not play a role in
246 inhibition of IFN-I production. M has also been reported to inhibit the induction of ISGs
247 downstream of the IFN-I receptor [30]. M WT, as well as the mutants M-K14R, M-K15R,
248 and M-KallR reduced the IFN-induced ISRE luciferase reporter activity (Fig. S2m),
249 suggesting that ubiquitination of the lysine residues is not necessary for antagonism of
250 IFN-I signaling.
251 Taken together, the increased IFN response observed in *Trim7*^{-/-} mice is unlikely to be
252 mediated by M ubiquitination and does not explain the increased virus replication
253 observed in the knockout mice.
254
255 **TRIM7 promotes innate immune inflammation while protecting from cell death**
256 **during SARS-CoV-2 infection**
257 TRIM7 has been associated with the induction of genes involved in cell growth,
258 proliferation, and survival [45]. Conversely, SARS-CoV-2 has been shown to induce cell
259 death in lung cells [46], and its M protein has been associated with apoptotic effects [17]. At
260 day 3 post-infection, we observed a significantly higher proportion of cells positive for
261 Apotracker staining (cells undergoing apoptosis) in the lungs of *Trim7*^{-/-} mice as
262 compared to WT controls (Fig. 3a). These effects were evident in CD45^{-} cells (Fig. 3b-c
263 and S3a-c). In contrast, no differences were observed in apoptosis between WT and KO
264 mice within the hematopoietic CD45^{+} compartment (Fig. S3b).
265 We evaluated whether TRIM7 antiviral effects were associated with changes in the
266 innate immune cell composition in the lungs. *Trim7*^{-/-} mice showed reduced neutrophil
267 and monocyte infiltration as compared to WT mice at day 3 p.i. (Fig. 3d-e and S3c),
268 whereas no differences in infiltration of plasmacytoid DCs (pDCs) were observed (Fig.
269 3f). Multiplex analysis of lung and serum cytokines showed reduced pro-inflammatory
270 cytokines IL-6, IL-1β, and IL-1α in *Trim7*^{-/-} mice (Fig. 3g and S4a-b). In line with the
271 reduced cellular infiltration to the lung, the neutrophil chemoattractant CXCL1 in serum
272 was lower in *Trim7*^{-/-} mice as compared to controls (Fig. 3h). In further support of the
273 role of TRIM7 in promoting immune inflammation, RNAseq and Gene Ontology analysis
274 (GO) of infected lungs showed that downregulated genes were enriched in pathways
275 related to the inflammatory response (neutrophil degranulation, innate immune
276 signaling, and cytokine signaling) as well as cell division/survival (mitotic genes) (Fig.

277 3i). Specifically, induction of *Il6*, *Il1b*, *Cxcl1*, *Tnfaip6*, and *Mmp8* was reduced in *Trim7*$^{-/-}$
278 mice (Fig. 3j). These results correlate at the protein level of IL-6 in the lung (Fig. S4c-d)
279 and CXCL1 in the serum.
280 Since we found a lower number of neutrophils in the lungs of *Trim7*$^{-/-}$ mice, we asked
281 whether neutrophil recruitment to the lung could be associated with protection from
282 disease. To test this, C57BL/6J WT mice were depleted of neutrophils (Fig. S4e). Anti-
283 Ly6G-treated mice lost weight at a similar rate as isotype-treated mice until the peak of
284 viral titers (day 3 p.i.). However, neutrophil-depleted mice recovered from infection
285 significantly slower than control mice (Fig. 3k). These effects did not appear to be due to
286 differences in virus replication because control and neutrophil-depleted mice showed
287 similar virus titers (Fig. 3l). These data suggest that neutrophils are not responsible for
288 the antiviral role mediated by TRIM7 but may be involved in tissue repair/healing during
289 the recovery phase. In support of this, neutrophil-depleted mice had a significantly
290 higher frequency of apoptotic cells, specifically in the CD45$^-$ compartment (Fig. 3m-n),
291 suggesting that neutrophils are important for the removal of apoptotic cells either
292 directly or indirectly, promoting tissue repair during the recovery phase.
293 Overall, our data indicate that TRIM7 is antiviral during SARS-CoV-2 infection and
294 suggest that TRIM7 regulates inflammatory immune responses.
295
296 **TRIM7 protects from SARS-CoV-2-induced apoptosis and requires an intact K14**
297 **residue on M**
298 Apoptosis during viral infection is a process that can either limit virus replication or
299 promote virus dissemination [47]. To evaluate the relationship between M, TRIM7, and
300 apoptosis, WT and TRIM7 KO A549 cells were transfected with vectors expressing WT
301 or M mutants. Upon transfection of WT M, a significantly higher frequency of apoptotic
302 cells was observed in TRIM7 KO cells as compared to WT cells. These effects required
303 the presence of an intact K14 residue on M because expression of an M-K14R mutant
304 that cannot be ubiquitinated by TRIM7 induced higher frequency of cells in apoptosis in
305 WT cells, and no further difference was observed in TRIM7 KO cells (Fig. 4a-b, controls
306 for expression shown in Fig. S5a). TRIM7 KO cells also display reduced AKT
307 phosphorylation upon stimulation with TNF, while no differences were observed in
308 IKKα/β phosphorylation (Fig. S5b), providing further evidence that TRIM7 is involved in
309 signaling pathways associated with apoptosis and cytokine signaling. Overall, these
310 data suggest that TRIM7 protects from cell apoptosis via ubiquitination on the K14
311 residue and this potentially reduce virus replication.
312
313 **SARS-CoV-2 Membrane protein mutations on K14 appeared during the pandemic**
314 **in COVID-19 patients**
315 We next asked whether mutations that lead to loss of ubiquitination and cause more
316 apoptosis can appear in circulating strains of SARS-CoV-2. Data analysis from all ~8.5
317 million SARS-CoV-2 genomes present in GenBank from the beginning of the pandemic
318 to March 2024, was performed with CoV-Spectrum [48]. From the samples analyzed, we
319 observed that 985 showed mutations on K14 residue representing 0.01% of the total
320 samples. Mutations on this site were relatively more frequent early in the pandemic, with
321 a higher occurrence (~0.95%) in samples from clade 19A (Fig. 4c). The most common
322 mutation was a deletion of K14, followed by the K14R mutation (Fig. 4d and Table 1).

7

323   The mutations on the K15 residue were more frequent, present in 0.02% of associated
324   samples in GenBank (2433), Fig. 4e and Table 2). Samples with K14 and K15
325   mutations were more infrequent, being observed 51 times in total, with all except one of
326   these double mutations being a double deletion (and Table 3). This analysis shows that
327   these mutations can occur in nature and were overrepresented in early clades during
328   the pandemic.
329
330   **A recombinant virus with M K14/K15 mutations causes more apoptosis in mice**
331   Since we are unable to correlate these mutations with clinical data from patients, we
332   tested the relevance of these mutations in viral pathogenesis in a mouse model. To this
333   end, we generated a recombinant mouse-adapted double mutant virus M-K14/K15R
334   (CMA5 M-K14/15R), which cannot be ubiquitinated on either K14 or K15 sites. We used
335   this double mutant to avoid generating a virus with increased replication ability due to
336   the loss of the target site for TRIM7 ubiquitination. Since previous studies have shown
337   that ubiquitination on M-K15 by another E3-Ub ligase, RNF5, is required for efficient
338   virus release [40], introducing the K15R mutation on the K14R mutant virus should result
339   in an attenuated virus. This would still allow us to dissect the roles of ubiquitination on
340   virus replication and apoptosis by both the K14 and K15 residues of M.
341   As predicted, this M-K14/K15 mutant virus showed reduced replication kinetics in the
342   IFN-incompetent Vero E6 as well as in IFN-competent Calu-3 cell lines, as compared to
343   the parental WT virus (Fig. 5a, 5c, S6a and S6c). Consistent with the role of K15 in virus
344   particle formation and budding [40], the viral RNA accumulated in the cells at similar rates
345   between the K14/15R and the parental virus strain (Fig. 5b, 5d, S6b, 6d). Since Vero
346   cells do not produce active IFN-I, the differences observed are likely not IFN-I
347   dependent. Consistent with this, no difference in ISG54 mRNA levels was observed
348   between the parental and the mutant virus in Calu-3 cells (Fig. S6e). These data
349   contrast with the phenotype we observed of enhanced virus replication in *Trim7*^{-/-} mice
350   but can be explained by the loss of ubiquitination on M-K15 that is required for virus
351   release. Importantly, even though the M-K14/15R mutant virus is highly attenuated, it
352   showed a higher ratio of cells in apoptosis when normalized by PFU (Fig. 5e). Similarly,
353   the M-K14/15R virus replicated to lower levels in the lungs of WT mice (Fig. 5f) but
354   caused increased weight loss (Fig. 5g), and increased apoptosis as compared to the
355   WT parental virus (Fig. 5h and S6f-g). No differences in the production of IFN-β or
356   ISG54 were observed in the lung at day 3 p.i. (Fig. S6h-i). Together, these data and the
357   data described above suggest that the K15 site promotes virus replication while the K14
358   site protects cells from apoptosis during SARS-CoV-2 infection.
359   Next, we examined whether TRIM7 can still inhibit virus replication in the absence of the
360   K14/K15 ubiquitination sites. As expected, overexpression of TRIM7 in 293T-hACE2
361   cells reduced replication of the parental WT virus (Fig. 5i). In contrast, overexpression of
362   TRIM7 did not significantly reduce replication of the K14/15R virus as compared to the
363   empty vector control (Fig. 5i). The mutant virus showed reduced replication as
364   compared to the parental virus, confirming that this mutant virus is attenuated.
365   Overexpression of the inactive TRIM7-ΔRING did not affect the replication of either virus
366   and served as an additional control (Fig. 5i). In line with these results, while the parental
367   WT virus replicated to higher levels in *Trim7*^{-/-} compared to WT mice, no significant
368   difference was observed when comparing M-K14/15R titers between WT and *Trim7*^{-/-}

369 mice (Fig. 5j). The loss of the K14 ubiquitination site, which is mediated by TRIM7,
370 would explain the lost difference between WT and KO mice. The K14/15R virus still
371 replicated to a lower titer than the WT virus in *Trim7*^{-/-} mice and this can likely be
372 explained by the loss of the K15 ubiquitination site, which is dependent on RNF5 and
373 not TRIM7. The loss of ubiquitination on K14/15 resulted in a slight increased number of
374 cells in the lung undergoing apoptosis as compared to the parental virus in WT mice. As
375 expected, the parental virus promoted greater levels of apoptosis in *Trim7*^{-/-} mice,
376 however the M-K14/15R mutant virus did not (Fig. 5k). These data suggest that TRIM7
377 restricts apoptosis in the lung during SARS-CoV-2 infection and this requires intact
378 K14/15 residues on the M protein.
379
380 **TRIM7 mediates its antiviral effects by inhibiting caspase-6 activation**
381 Apoptosis during viral infection is known to play an important role in limiting virus
382 replication [49,50]. Intriguingly, coronaviruses can take advantage of the apoptosis
383 machinery to promote their replication [51,52]. Therefore, we evaluated if TRIM7's antiviral
384 mechanism depends on its ability to inhibit apoptosis. To test this, we used inhibitors of
385 apoptosis, Z-VAD-FMK (a pan caspase inhibitor), and Z-VEID-FMK, (which targets
386 caspase-6 and has been shown to inhibit SARS-CoV-2 replication [51]). Consistent with
387 this previous study, treatment with caspase-6 inhibitor (Z-VEID-FMK) strongly reduced
388 replication of both the parental and the M-K14/15R viruses in 293T-hACE2 cells (Fig.
389 6a) and completely inhibited apoptosis (Fig. S6j). However, while overexpression of
390 TRIM7 reduced viral titers in DMSO-treated cells, TRIM7 lost its ability to further reduce
391 SARS-CoV-2 replication as compared to vector control in cells treated with Z-VEID-FMK
392 or Z-VAD-FMK (Fig. 6a and expression controls in Fig. S6k). This suggests that TRIM7
393 requires, at least in part, an active caspase-6 pathway to exert its antiviral activity. Since
394 it has been shown that caspase-6 can cleave N protein of coronaviruses [52-54] and
395 cleaved N inhibits the IFN-I response leading to increased virus replication, we
396 evaluated if TRIM7 is involved in the cleavage of N. Treatment with staurosporine
397 (STS), which activates apoptotic pathways, enhanced cleavage of N as compared to
398 vehicle control in WT A549 cells. These effects were further increased in TRIM7 KO
399 cells, in which additional products of N cleavage were evident (Fig. 6b). These effects
400 correlated with slightly enhanced cleavage of caspase-6 in TRIM7 KO cells (Fig. 6b). In
401 support of these results, WT mice treated with Z-VEID-FMK show less weight loss (Fig.
402 6c) and significantly reduced viral titers in the lungs as compared to DMSO-treated mice
403 (Fig. 6e). In contrast, Z-VEID-FMK treatment of *Trim7*^{-/-} mice did not prevent weight loss
404 (Fig. 6d), indicating that TRIM7 deficient mice are more resistant than WT mice to the
405 protective effects of the inhibitor. Importantly, treatment with Z-VEID-FMK reduced virus
406 titers in the *Trim7*^{-/-} mice to the levels observed in the DMSO-treated WT animals (Fig.
407 6e), suggesting that the antiviral activity of TRIM7 is, in part, mediated by inhibition of
408 caspase-6 activity. Notably, TRIM7 also shows antiviral activity *in vivo* that is
409 independent of caspase-6, because *Trim7*^{-/-} mice treated with the inhibitor have
410 significantly higher viral titers compared to WT-treated mice (Fig. 6e).
411 In line with the proposed role of N cleavage in IFN antagonism, WT mice treated with Z-
412 VEID-FMK showed higher levels of IFN-β and ISG54 mRNA in infected lungs,
413 suggesting that the caspase-6 inhibition indeed results in increased IFN responses that
414 could potentially inhibit virus replication, in WT mice. Surprisingly, these effects did not

9

415 recapitulate in *Trim7-/-* mice. Consistent with our data described above, vehicle control
416 treated *Trim7-/-* mice showed higher IFN responses than WT mice, however caspase
417 inhibition in *Trim7-/-* did not increase but rather reduced IFN/ISGs (Fig. 6f-g). These data
418 suggest that TRIM7 limits virus replication via a mechanism that partially requires
419 inhibiting caspase-6 activity, but it is mostly independent of IFN-I.
420
421 **Discussion**
422 In this study, we show that TRIM7 has antiviral activity against SARS-CoV-2 by
423 ubiquitinating the K14 residue on M, and these effects are associated with reduced
424 apoptosis during infection. Our experiments using caspase inhibitors suggest that the
425 antiviral effects of TRIM7 require an active caspase-6 pathway, linking apoptosis to
426 virus replication and pathology. While our study is in line with a previous report that
427 coronaviruses use apoptosis to replicate [51], in our study the effects do not seem to be
428 dependent on IFN-I. Although TRIM7 depletion does result in increased cleavage of the
429 viral protein N as well as increased IFN-I induction, these effects do not lead to reduced
430 virus replication. Furthermore, blocking IFN-I signaling did not change virus titers,
431 further suggesting that in this model IFN-I does not play an antiviral role. In previous
432 studies in mice, IFN-I has been associated with pathology [24]. Our data agree with these
433 studies, in which IFN-I seems pathogenic and not a major antiviral mechanism. Higher
434 levels of IFN produced by the *Trim7-/-* mice do not reduce virus titers to the levels
435 observed in WT mice. Intriguingly, blocking IFN-I signaling in the *Trim7-/-* mice, which
436 induces higher IFN responses, does not affect weight loss (Fig. S6l), although it does
437 result in increased virus titer as compared to isotype-treated *Trim7-/-* mice (Fig. S6m).
438 This suggests that there is a threshold for IFN-I to have antiviral effects, but without
439 affecting pathology. Therefore, the increased disease phenotype observed in *Trim7-/-*
440 mice is IFN-I independent.
441   At the moment the connection between cleavage of N and the increased virus
442 replication observed in *Trim7-/-* mice remains unclear. However, it is clear that TRIM7
443 and M-K14 are associated with inhibiting the caspase-6 pathway to inhibit virus
444 replication.
445 Our data also indicate that ubiquitination on M-K14 leads to opposite effects from those
446 of the ubiquitination mediated by RNF5 on M-K15, which has a proviral activity [40]. We
447 further confirmed the previously proposed proviral role of K15, using a recombinant
448 mutant virus.
449 Although we cannot completely rule out that ubiquitination on K15 can also contribute to
450 effects on apoptosis, our data suggest that ubiquitination on both residues is not
451 mutually exclusive. Using structures of the M protein in its long and short form, we
452 modelled ubiquitinated forms of M with ubiquitin covalently attached to either K14 and/or
453 K15, our structural modeling analysis suggests that ubiquitination of both lysine
454 residues is energetically possible, either with covalent ubiquitination to one lysine in
455 each M protein monomer, or even with ubiquitination happening in neighboring residues
456 of the same chain (Fig. S7a-d). Our calculations indicate that there is a small energetic
457 advantage for the long form of M, suggesting that ubiquitination may drive the
458 population ensemble of M towards the long form.
459 The advantage of using this double mutant virus is that we can avoid any compensatory
460 ubiquitination on one residue if the neighboring one is missing. We also show that these

461 mutations do not affect the IFN-I response and it is unlikely that the effects on virus
462 replication are IFN-I mediated.

463 We observed a dysregulation in the inflammatory response in the *Trim7*^{-/-} mice with a
464 reduced number of infiltrating neutrophils and monocytes in the lung. Inflammatory
465 monocytes responsible for producing inflammatory cytokines such as IL-6, TNF-α, and
466 IL-1β are recruited to the lung in patients with COVID-19. These cytokines have been
467 associated with detrimental inflammation but can also have protective roles [58-60]. In this
468 mouse model, the decreased levels of proinflammatory cytokines in *Trim7*^{-/-} mice may
469 correlate with dysfunctional activation of the inflammatory responses associated with
470 severe COVID-19 patients [59,61-63]. Furthermore, a decrease in monocytes in *Trim7*^{-/-}
471 correlated with an increase in viral load, consistent with the finding that reduction of
472 monocyte recruitment in *ccr2*^{-/-} mice increases virus in the lungs and also increased
473 IFN-I RNA during infection [64].

474 In addition, neutrophils have been associated with pathology through the induction of
475 Neutrophil Extracellular Traps (NETs)[65-67]. Our data suggest that the reduction of
476 neutrophils in *Trim7*^{-/-} mice is not the reason for the increased virus titers but could
477 contribute to the increased apoptosis. Neutrophils appear to play an important
478 protective role in the recovery phase and could be associated with healing and
479 protecting from apoptosis. This is in line with studies showing that neutrophils can be
480 involved in tissue repair by MMP-9, which can regulate activation of PRRs and promote
481 angiogenesis [68-72], and is relevant given the degree of damage to blood
482 vessels/endothelialitis in COVID-19 [73]. These effects could be mediated by a specific
483 subpopulation of neutrophils that needs further characterization, that could also
484 potentially be important for the removal of apoptotic bodies or possibly indirectly by
485 recruiting other cells responsible for this clearance.

486 Together, our data show that TRIM7 is an important regulator of the innate immune
487 inflammatory response that protects against SARS-CoV-2. TRIM7 also negatively
488 regulates MDA5 signaling, which may help control the detrimental inflammatory effects
489 of IFN-I [74] (Fig. S8). Finally, we identified that mutations on residues K14 and K15 can
490 occur in the circulating strains of SARS-CoV-2. Although the presence of these
491 mutations is relatively low and does not correlate with a specific variant of concern
492 (VOC), the presence of these mutations could indicate that these strains are potentially
493 more pathogenic. Therefore, we propose that monitoring mutations on M in infected
494 individuals might predict disease severity if the effects can be correlated with clinical
495 profiles in infected patients.

496
497
498
499
500
501
502
503
504
505
506

11

507
508
509
510

Acknowledgements

512

517

Author contributions

519 MG-O. performed all aspects of this study. H.X. generated mutant virus. H-c.T. and A.O.
520 performed *in vivo* experiments. A.H., P.B., K.A., M.I.G., M.H., L.P-C., Y.P-T. and S.v.T.
521 performed *in vitro* experiments. M.C. and M.B. performed global analysis of sequences.
522 N.T. and R.J.N. performed the computational modeling analysis. T.R.S. performed
523 histopathological analysis. R.S. V.M., M.E., J.E., P-Y.S., X.X., A.F. provided critical
524 reagents and technical advice. R.R. designed, directed, contributed with data analysis,
525 and obtained funding. M.G-O. and R.R. organized the study and prepared the
526 manuscript. All authors read the manuscript and provided comments.

527

Declaration of interest

529 The authors declare no competing interests.

530

Resource availability

532 Further information and requests for resources and reagents should be directed to and
533 will be fulfilled by the corresponding author, Ricardo Rajsbaum
534 (ricardo.rajsbaum@rutgers.edu)

Materials availability

536 Plasmids generated in this study are available upon request from the corresponding
537 author.

Data availability

539 Transcriptomic data generated during this study has been deposited with the NCBI
540 Gene Expression Omnibus (GEO) database under: GSE268640 accession number.

541
542
543
544
545
546
547

METHODS

Cell culture

HEK293T (CRL-11268), and A549 (CCL-185) cell lines were purchased from ATCC. Calu-3 2B4 cells were kindly provided by Vineet D. Menachery (The University of Texas Medical Branch at Galveston) [75] Vero E6 cells were kindly provided by Pei-Yong Shi (The University of Texas Medical Branch at Galveston). HEK293T-hACE2 cells were kindly provided by Benhur Lee (Mount Sinai) [76]. A549 TRIM7 KO cells were generated as described by [37]. All cells were maintained in Dulbecco's Modified Eagle's Medium (DMEM) (GIBCO) supplemented with 10% v/v fetal bovine serum (FBS) (HyClone) and 1% v/v penicillin-streptomycin (Corning) in a humidified 5% CO_2 incubator at 37˚C.

Viruses

Viruses used in this study were handled under biosafety level 3 (BSL-3) conditions at UTMB facilities in accordance with institutional biosafety approvals. SARS-CoV-2 (USA-WA1/2020) was kindly provided by The World Reference Center of Emerging Viruses and Arboviruses (WRCEVA) (The University of Texas Medical Branch at Galveston), SARS-CoV-2 (CMA3p20) was kindly provided by Vineet D. Menachery (The University of Texas Medical Branch at Galveston) and grown in Vero E6 cells as described by Muruato, et al. 2021 [42]. SARS-CoV-2 USA-WA1/2020+ D614G was provided by Dr. Pei-Yong Shi (The University of Texas Medical Branch at Galveston).

The infectious cDNA clone icSARS-CoV-2 M-K14/15R was constructed through mutagenesis of a mouse-adapted USA-WA1/2020 SARS-CoV-2 (CMA5 strain) used for in vivo studies [77,78]. To generate the CMA5 strain, an adaptive mutation (Spike_Q493H) was identified and engineered into the backbone of the CMA3p20 strain [42]. The full-length cDNA was assembled via *in vitro* ligation and used as a template for T7 *in vitro* transcription. The full-length viral RNA was electroporated into Vero E6 cells. 48 hours post electroporation, the original P0 virus was harvested and used to infect another flask of Vero E6 cells to produce the P1 virus. The titer of the P1 virus was determined by plaque assay on Vero E6 cells. The viral RNA of P1 virus was extracted and sequenced to confirm the designed mutations using the primers: M-K14R/K15R-F-ACCGTTGAAGAGCTTCGCCGCCTCCTTGAACAATGG and M-K14R/K15R-R CCATTGTTCAAGGAGGCGGCGAAGCTCTTCAACGGT. The P1 virus was used for all the experiments performed in this study. All work following electroporation was performed in a BSL3 laboratory.

Plasmids

The M-WT, M-K14R, M-K15R, M-KallR, and M-K14O were cloned into pXJ-HA plasmid, Flag-TRIM7 constructs Variant 1 and 2 were purchased from Origene (Rockville, MD), the Flag-OTU and -OTU2A were kindly provided by Adolfo Garcia-Sastre (Mount Sinai), the Ub plasmids have been described before [79].

Transfections

Transient transfections of DNA were performed with TransIT-LT1 (Mirus Bio) for HEK293T cells, and Lipofectamine 3000 (Invitrogen) for A549 cells according to the

13

593 manufacturer's guidelines. For lipofectamine transfection media was exchanged 6-8 hrs.
594 All transfections were performed in DMEM 10% v/v FBS without penicillin-streptomycin.
595

Cell lysis and co-immunoprecipitation
597 Cells were harvested in RIPA lysis buffer (50 mM Tris-HCl, pH 8.0, 150 mM NaCl, 1%
598 (v/v) IGEPAL CA-630, 0.5% (w/v) sodium deoxycholate, 0.1% (v/v) SDS, protease
599 inhibitor cocktail [80], 5 mM N-ethylmaleimide (Sigma), and 5 mM iodoacetamide (Sigma)
600 as deubiquitinase inhibitors. Cell lysates were clarified by centrifugation at 21,000 x g
601 for 20 min at 4C. 10% of the clarified lysate was added to 2X SDS-PAGE loading buffer
602 containing 2- Mercaptoethanol, heated for 30 min at 37°C, and stored at -20°C as a
603 whole-cell lysate (WCL). The remaining lysate was subjected to immunoprecipitation
604 with anti-FLAG M2 or anti-HA, EZview Red agarose beads (Sigma) overnight at 4°C on
605 a rotating platform. Beads were washed seven times in RIPA buffer (150 or 550 mM
606 NaCl) and the bound proteins were eluted using FLAG or HA peptide respectively,
607 elution was reduced in 2X SDS-PAGE loading buffer containing 2- Mercaptoethanol and
608 incubated for 30 min at 37°C.
609

Denaturing pull-down
611 Cell lysis and WCL collection were performed as above. Lysates were subjected to pull
612 down using nickel-nitrilotriacetic acid (Ni-NTA) beads (Qiagen) overnight at 4 °C on a
613 rotation platform. Beads were washed seven times using denaturing buffer containing
614 50mM Tris HCl pH8.0 (Sigma), 6M urea, 350 mM NaCl, 0.5%(v/v) IGEPAL CA-630
615 (Sigma) and 40mM imidazole (Sigma). The proteins were eluted at 4 °C for 30 min,
616 using elution buffer containing 50mM Tris-HCl pH8.0 and 300mM imidazole. Eluted
617 proteins were treated with in 2X SDS-PAGE loading buffer containing 2-
618 Mercaptoethanol and incubated for 30 min at 37°C.
619

Confocal Immunofluorescence
621 HeLa cells were seeded into 6-well plates. After 16h, the cells were transfected with 1μg
622 of M WT or M-K14R-HA tagged with the co-expression of TRIM7-FLAG tagged for 24h.
623 The cells were washed with DPBS 1X, fixed with 4% paraformaldehyde 20',
624 permeabilized with 0.1% Triton X100 (v/v) in DPBS 1X for 5 minutes, and blocked with
625 0.5% pork skin gelatin (w/v) in DPBS for 1h. The staining was performed with rabbit
626 anti-HA (Milipore Sigma H6908, 1:100 dilution), anti-FLAG (Sigma-Aldrich F1804, 1:100
627 dilution in P) overnight at 4°C. The next day, cells were washed with DPBS 1X and
628 incubated with the secondary antibodies anti-mouse Ig Alexa Fluor 488 (Invitrogen
629 A21202) and anti-rabbit Ig Alexa Fluor 555 (Invitrogen A31572) at 1:200 dilution each in
630 DPBS 1X and washed with DPBS 1X after 2h incubation at RT. DAPI staining (Bio
631 Legend) working solution (1μg/mL in PBS) was added for 5 minutes at RT and washed
632 with PBS before mounting with Merck FluorSave™ reagent. Micrographs were taken
633 with the Leica Stellaris 8 tau-STED Microscope (Leica Microsystems). Microscope
634 parameters and LAS-X software post-processing were set constant for each
635 experiment. Fluorescence intensity values were obtained with ImageJ software
636 (National Institute of Health) and curves were graphed with Graphpad Prism 10
637 (Graphpad Software, Inc.).
638

Virus-like particles (VLPs) generation

VLPs were generated by transfection of the plasmids for expression of S-HA, M-HA, N-FLAG, and E-FLAG, into A549 WT and TRIM7 knockout, briefly; 2×10^5 cells were seeded into a 6-well plate and transfected using a total of 2 µg of plasmid using Lipofectamine 3000 (Invitrogen, USA) as per the manufacturer's instruction. The molar ratio for the S, E, M, and N plasmid was 8:8:6:3 as described by [81]. 70h after transfection the supernatant was collected, and the cells were harvested in RIPA buffer for immunoblotting. The supernatant was clarified by centrifugation 4000 rpm for 10 minutes, then the supernatant was filtered through a 0.45 µM mesh to remove the debris, subsequently, the supernatant was layered over in a 20% sucrose gradient and ultra-centrifugated at 25,000 rpm for 3h at 4°C to pellet down the VLPs and subsequently loaded on to discontinuous, 20–60% sucrose solution and centrifuged at 25,000 rpm for 3 h at 4°C. The opaque band containing the VLPs were collected and analyzed by western blot.

Western blot

Cell lysates were resolved on 7.5 or 4–15% Mini-PROTEAN and Criterion TGX SDS-PAGE gels and transferred to polyvinylidene difluoride (PVDF) membranes using a Trans-Blot Turbo transfer system (Bio-Rad). Membranes were blocked with 5% (w/v) non-fat dry milk in TBST (TBS with 0.1% (v/v) Tween-20) for 1h and then probed with the indicated primary antibody in 3% (w/v) BSA in TBST at 4°C overnight. Following overnight incubation, membranes were probed with secondary antibodies in 5% (w/v) non-fat dry milk in TBS-T for 1 h at room temperature in a rocking platform: anti-rabbit or anti-mouse IgG-HRP conjugated antibody from sheep (both 1:10,000 NA934 and NA931 GE Healthcare). Proteins were visualized using ECL or SuperSignal West Femto chemiluminescence reagents (Pierce) and detected by autoradiography.

Mice

All animal experiments were carried out following Institutional Animal Care and Use Committee (IACUC) guidelines and have been approved by the IACUC of the University of Texas Medical Branch at Galveston. Our studies utilized 20- to 25-week-old C57BL/6NJ WT mice (The Jackson Laboratory) that match the *Trim7-/-* mice generated as described by [37] and 25-week-old C57BL/6J WT mice (The Jackson Laboratory). Mice were maintained under specific pathogen-free conditions in the Animal Resource Center (ARC) facility at UTMB. Animal experiments involving infectious viruses were performed under animal biosafety level 3 (ABSL-3) conditions at UTMB in accordance with institutional biosafety approvals.

***In vitro* virus infection**

HEK293t-ACE-2 overexpressing TRIM7 or TRIM7ΔRING domain were seeded onto 24-well plates at a confluency of 100,000 cells/well and infected with SARS-CoV-2 USA/WA-1 D614G strain MOI 0.1 for 1h, cells were washed once with DPBS 1X and incubated with 6, 24 and 48h after infection. supernatant, RNA, and protein were collected to measure virus titers, gene, and protein expression respectively.

In vivo virus infection

WT and *Trim7* $^{-/-}$ mice were anesthetized with 5% isoflurane and infected intranasal with SARS-CoV-2 1×10^6 PFU of CMA3p20 strain, mice were weighed every day for 7 days. Euthanasia was performed at days 2, 3, or 7 post-infection using isoflurane overdose, lungs and serum were collected for downstream analysis. For neutrophil depletion experiments WT C57BL/6J mice were injected intraperitoneally [82] with 100μg/mouse of anti-Ly6G or isotype (BioXCell) one day before and one after the infection, mice were infected with SARS-CoV-2 1×10^6 PFU of CMA3p20 and weighed every day for 10days. At Day 3 post-infection a group of mice was euthanized to perform flow cytometry of lung or peripheral blood to confirm neutrophil depletion. For caspase-6 inhibition experiments C57BL/6NJ mice were treated with Z-VEID-FMK (APExBIO), dose: 12.5mg/kg diluted in PBS or DMSO in PBS as the vehicle through IP injection at day 0, 1, and 2 post-infection. For IFN-I blocking experiments mice were IP injected with or IFNAR1 Isotype IgG control antibody 2mg/per mice at day 0.

Lung single-cell suspension and flow cytometry

Lungs isolated from infected mice were collected in RPMI 10% v/v FBS 1% v/v penicillin-streptomycin, lungs were rinsed with DPBS cut into small pieces and digested in digestion media containing collagenase D 0.7mg/ml and DNase I 30μg/ml in serum-free RPMI for 30 minutes in a humidified 5% CO_2 incubator at 37°C. FBS was added to the digestion media to inactivate the enzymes. Lungs were then passed through 70μm cell strainer to obtain single-cell suspension. Red blood cells were lysed using RBC lysing buffer Hybri-Max (Sigma), cells were counted and 1×10^6 cells were stained using the following antibodies. Anti-CD45-PE(Biolegend), Anti-Podoplanin PE-DAZZLE594 (Biolegend), Anti-CD24-BUV395 (BD Biosciences) Anti-CD31-BV510, Anti-CD326-BV711 (Biolegend), Anti- MHC-II-BV605 (Biolegend), or Anti- PDCA-1-APC, Anti- CD11b-AF700, Anti- Ly6G-BV780, Anti-CD11c Percp-Cy5.5, Anti- Ly6C-FITC. To measure cell death and apoptosis, cells were stained with Ghost dye-Red780(Tonbo Biosciences) or Fixable viability dye-eFluor506(eBiosciences) and Apotracker Green (Biolegend). After staining samples were fixed using 4% ultrapure formaldehyde diluted in DPBS from 16% methanol-free ultrapure formaldehyde (Thermo Scientific) for 48h. Samples were acquired using LSR II Fortessa and analyzed using FlowJo.

Plaque Assay

The supernatant of infected cells or lung homogenate was used to measure viral titers. Briefly, confluent monolayers of Vero E6 cells plated in a 12-well plate were infected with virus diluted using DMEM 2% v/v FBS without penicillin-streptomycin, incubated at 37°C for 1h rocking the plate every 15 minutes. Infectious were removed and media was replaced with MEM containing 0.6% v/v tragacanth (Sigma), 5% v/v FBS and 1% v/v penicillin-streptomycin, plates were incubated at 37°C for 2 days in humidified 5% CO_2 incubator. Plates were fixed and stained using 10% buffered formalin containing 0.5% (w/v) crystal violet for 30 minutes.

Histology

The right inferior lobe of the lung was fixed in 10% neutral buffered formalin (HT501128, Sigma, MI) for 7 days. Tissues were cut, paraffinized and H&E stained by the Anatomic

731 Pathology Laboratory of the Pathology Department of University of Texas Medical
732 Branch. The inflammatory score was calculated by analyzing the presence of
733 peribronchiolar infiltrates (Yes=1, No=0) plus 1-2 Foci of inflammation (1), 2-3 foci of
734 inflammation (2) and 3+ foci of inflammation [83].
735

IFN-β or ISRE luciferase reporter assay
737 HEK293T cells were seeded into 24-well plates (50,000 cells/well) and were transfected
738 with 30 ng of IFN-β or 180 ng of ISRE reporter plasmid together with 10 ng of Renilla
739 luciferase plasmid. For IFN-β reporter assay cells were co-transfected with 5 ng of
740 MDA5 and increasing concentrations of TRIM7 20,40 or 80 ng for 24hrs. for ISRE
741 assays cells were co-transfected with 100 ng of M WT or K-R mutants plasmids for 24h
742 and stimulated with 1000IU/ml of IFN-β for 16h. Cells were lysed and luciferase activity
743 was measured using the DualLuciferase reporter assay system (Promega) on a
744 Cytation 5 Multi-Mode Reader (BioTek) according to the manufacturer's instructions.
745 Values were normalized to Renilla.
746

Quantitative reverse-transcription-PCR (qRT-PCR)
748 Total RNA was isolated using the Direct-zol RNA Miniprep Kit (Zymo Research)
749 following the manufacturer's instructions. Reverse transcription was performed using
750 the High-Capacity cDNA Reverse Transcription Kit (Applied Biosystems). Real-time
751 qPCR was performed in 384-well plates using iTaq Universal SYBR Green Supermix
752 and a CFX384 Touch Real-Time PCR Detection System (Bio-Rad). Gene expression
753 was normalized to either human 18S or murine β-actin by the comparative CT method
754 (DDCT).
755

Cytokine quantification
757 Cytokines from serum and lung homogenate were quantified using Bio-Plex mouse
758 cytokine 23-plex assay (BioRad) following the manufacturer's instructions. Serum was
759 diluted 1:3. Samples were analyzed in a Bio-Plex200 Multiplex system (Bio-Rad).
760

Global Analysis
762 Global membrane protein K14/K15 mutation occurrence was analyzed using the CoV-
763 Spectrum [48] (https://open.cov-spectrum.org) dashboard. The analysis covered all
764 samples in the "Open Data" version of CoV-Spectrum (GenBank deposited samples)
765 and the period 2020-01-06 to 2024-01-31. The following queries were used to
766 determine the occurrence of mutations to K14/K15 and K14+K15 (using Nextstrain
767 Clade 21A as an example):
768 21A (Nextstrain clade) & M:K14
769 21A (Nextstrain clade) & M:K15
770 21A (Nextstrain clade) & M:K14 & M:K15
771 For each query, the total number of samples belonging to the underlying clade was
772 obtained, and the percentage of samples with the particular mutation was determined
773 using the "Substitutions and Deletions" section of the resulting CoV-Spectrum reports.
774 Data was visualized using an adaption of the nCoV Clades Schema
775 (https://github.com/nextstrain/ncov-clades-schema)[84] using Miro.
776

Methods for M protein + ubiquitin modeling

We utilized structures of the M protein in its long form (PDB 7VGR) and short form (PDB 7VGS). To model the membrane, we used a lipid composition reminiscent of the biological ER-Golgi intermediate compartment (ERGIC) [55] and employed the CHARMM-GUI membrane builder [85-87]. Subsequently, we generated four models of covalent interactions with a ubiquitin structure (PDB 2JF5), each representing interactions with K14 and K15 from either the same M protein monomer or different monomers, for both conformational states of M. These models were then subjected to minimization using the Yasara web server [56], followed by the calculation of the total energy of the systems utilizing adapted Surfaces functions [57].

18

REFERENCES

1. Lamers, M. M. & Haagmans, B. L. SARS-CoV-2 pathogenesis. *Nat Rev Microbiol* **20**, 270-284 (2022). https://doi.org:10.1038/s41579-022-00713-0

2. Martines, R. B. *et al.* Pathology and Pathogenesis of SARS-CoV-2 Associated with Fatal Coronavirus Disease, United States. *Emerg Infect Dis* **26**, 2005-2015 (2020). https://doi.org:10.3201/eid2609.202095

3. Yan, W., Zheng, Y., Zeng, X., He, B. & Cheng, W. Structural biology of SARS-CoV-2: open the door for novel therapies. *Signal Transduct Target Ther* **7**, 26 (2022). https://doi.org:10.1038/s41392-022-00884-5

4. Zhang, Z. *et al.* Structure of SARS-CoV-2 membrane protein essential for virus assembly. *Nat Commun* **13**, 4399 (2022). https://doi.org:10.1038/s41467-022-32019-3

5. Hou, Y. J. *et al.* SARS-CoV-2 Reverse Genetics Reveals a Variable Infection Gradient in the Respiratory Tract. *Cell* **182**, 429-446 e414 (2020). https://doi.org:10.1016/j.cell.2020.05.042

6. Tsatsakis, A. *et al.* SARS-CoV-2 pathophysiology and its clinical implications: An integrative overview of the pharmacotherapeutic management of COVID-19. *Food Chem Toxicol* **146**, 111769 (2020). https://doi.org:10.1016/j.fct.2020.111769

7. Delorey, T. M. *et al.* COVID-19 tissue atlases reveal SARS-CoV-2 pathology and cellular targets. *Nature* **595**, 107-113 (2021). https://doi.org:10.1038/s41586-021-03570-8

8. Sapir, T. *et al.* COVID-19 and the Immune Response: A Multi-Phasic Approach to the Treatment of COVID-19. *Int J Mol Sci* **23** (2022). https://doi.org:10.3390/ijms23158606

9. Yang, L. *et al.* COVID-19: immunopathogenesis and Immunotherapeutics. *Signal Transduct Target Ther* **5**, 128 (2020). https://doi.org:10.1038/s41392-020-00243-2

10. Ahn, J. H. *et al.* Nasal ciliated cells are primary targets for SARS-CoV-2 replication in the early stage of COVID-19. *J Clin Invest* **131** (2021). https://doi.org:10.1172/JCI148517

11. Sungnak, W. *et al.* SARS-CoV-2 entry factors are highly expressed in nasal epithelial cells together with innate immune genes. *Nat Med* **26**, 681-687 (2020). https://doi.org:10.1038/s41591-020-0868-6

12. Zou, X. *et al.* Single-cell RNA-seq data analysis on the receptor ACE2 expression reveals the potential risk of different human organs vulnerable to 2019-nCoV infection. *Front Med* **14**, 185-192 (2020). https://doi.org:10.1007/s11684-020-0754-0

13. Krishnamachary, B. *et al.* Extracellular vesicle-mediated endothelial apoptosis and EV-associated proteins correlate with COVID-19 disease severity. *J Extracell Vesicles* **10**, e12117 (2021). https://doi.org:10.1002/jev2.12117

14. Liu, Y. *et al.* Cell-Type Apoptosis in Lung during SARS-CoV-2 Infection. *Pathogens* **10** (2021). https://doi.org:10.3390/pathogens10050509

15. Li, X., Zhang, Z., Wang, Z., Gutierrez-Castrellon, P. & Shi, H. Cell deaths: Involvement in the pathogenesis and intervention therapy of COVID-19. *Signal Transduct Target Ther* **7**, 186 (2022). https://doi.org:10.1038/s41392-022-01043-6

16. Riegler, A. N., Benson, P., Long, K. & Leal, S. M., Jr. Differential activation of programmed cell death in patients with severe SARS-CoV-2 infection. *Cell Death Discov* **9**, 420 (2023). https://doi.org:10.1038/s41420-023-01715-4

866   17   Ren, Y. *et al.* SARS-CoV-2 Membrane Glycoprotein M Triggers Apoptosis With the
867   Assistance of Nucleocapsid Protein N in Cells. *Front Cell Infect Microbiol* **11**, 706252
868   (2021). https://doi.org:10.3389/fcimb.2021.706252
869   18   Yang, Y. *et al.* SARS-CoV-2 membrane protein causes the mitochondrial apoptosis and
870   pulmonary edema via targeting BOK. *Cell Death Differ* **29**, 1395-1408 (2022).
871   https://doi.org:10.1038/s41418-022-00928-x
872   19   Zhou, Z. *et al.* Heightened Innate Immune Responses in the Respiratory Tract of COVID-
873   19   Patients.   *Cell   Host   Microbe*   **27**,   883-890   e882   (2020).
874   https://doi.org:10.1016/j.chom.2020.04.017
875   20   Zhu, Q., Xu, Y., Wang, T. & Xie, F. Innate and adaptive immune response in SARS-CoV-2
876   infection-Current   perspectives.   *Front   Immunol*   **13**,   1053437   (2022).
877   https://doi.org:10.3389/fimmu.2022.1053437
878   21   Li, J., Zhang, K., Zhang, Y., Gu, Z. & Huang, C. Neutrophils in COVID-19: recent insights
879   and advances. *Virol J* **20**, 169 (2023). https://doi.org:10.1186/s12985-023-02116-w
880   22   Yu Zuo, S. Y., Hui Shi, Kelsey Gockman,Melanie Zuo, Jacqueline A. Madison, Christopher
881   Blair, Andrew Weber, Betsy J. Barnes, Mikala Egeblad, Robert J. Woods, Yogendra
882   Kanthi, and Jason S. Knight. Neutrophil extracellular traps in COVID-19. *JCI Insight* **5**
883   (2020). https://doi.org:https://doi.org/10.1172/jci.insight.138999.
884   23   Channappanavar, R. *et al.* Dysregulated Type I Interferon and Inflammatory Monocyte-
885   Macrophage Responses Cause Lethal Pneumonia in SARS-CoV-Infected Mice. *Cell Host*
886   *Microbe* **19**, 181-193 (2016). https://doi.org:10.1016/j.chom.2016.01.007
887   24   Israelow, B. *et al.* Mouse model of SARS-CoV-2 reveals inflammatory role of type I
888   interferon signaling. *J Exp Med* **217** (2020). https://doi.org:10.1084/jem.20201241
889   25   Yin, X. *et al.* MDA5 Governs the Innate Immune Response to SARS-CoV-2 in Lung
890   Epithelial   Cells.   *Cell   Rep*   **34**,   108628   (2021).
891   https://doi.org:10.1016/j.celrep.2020.108628
892   26   Sampaio, N. G. *et al.* The RNA sensor MDA5 detects SARS-CoV-2 infection. *Sci Rep* **11**,
893   13638 (2021). https://doi.org:10.1038/s41598-021-92940-3
894   27   Fu, Y. Z. *et al.* SARS-CoV-2 membrane glycoprotein M antagonizes the MAVS-mediated
895   innate   antiviral   response.   *Cell   Mol   Immunol*   **18**,   613-620   (2021).
896   https://doi.org:10.1038/s41423-020-00571-x
897   28   Sui, L. *et al.* SARS-CoV-2 Membrane Protein Inhibits Type I Interferon Production
898   Through Ubiquitin-Mediated Degradation of TBK1. *Front Immunol* **12**, 662989 (2021).
899   https://doi.org:10.3389/fimmu.2021.662989
900   29   Zheng, Y. *et al.* Severe acute respiratory syndrome coronavirus 2 (SARS-CoV-2)
901   membrane (M) protein inhibits type I and III interferon production by targeting RIG-
902   I/MDA-5   signaling.   *Signal   Transduct   Target   Ther*   **5**,   299   (2020).
903   https://doi.org:10.1038/s41392-020-00438-7
904   30   Xia, H. *et al.* Evasion of Type I Interferon by SARS-CoV-2. *Cell Rep* **33**, 108234 (2020).
905   https://doi.org:10.1016/j.celrep.2020.108234
906   31   Chen, K. *et al.* SARS-CoV-2 Nucleocapsid Protein Interacts with RIG-I and Represses RIG-
907   Mediated IFN-beta Production. *Viruses* **13** (2020). https://doi.org:10.3390/v13010047

20

908 32 Wu, J. *et al.* SARS-CoV-2 ORF9b inhibits RIG-I-MAVS antiviral signaling by interrupting
909   K63-linked   ubiquitination   of   NEMO.   *Cell   Rep*   **34**,   108761   (2021).
910   https://doi.org:10.1016/j.celrep.2021.108761
911 33 Lei, X. *et al.* Activation and evasion of type I interferon responses by SARS-CoV-2. *Nat*
912   *Commun* **11**, 3810 (2020). https://doi.org:10.1038/s41467-020-17665-9
913 34 Valerdi, K. M., Hage, A., van Tol, S., Rajsbaum, R. & Giraldo, M. I. The Role of the Host
914   Ubiquitin System in Promoting Replication of Emergent Viruses. *Viruses* **13** (2021).
915   https://doi.org:10.3390/v13030369
916 35 Xia, Y., Zhao, J. & Yang, C. Identification of key genes and pathways for melanoma in the
917   TRIM family. *Cancer Med* **9**, 8989-9005 (2020). https://doi.org:10.1002/cam4.3545
918 36 Fan, W. *et al.* TRIM7 inhibits enterovirus replication and promotes emergence of a viral
919   variant   with   increased   pathogenicity.   *Cell*   **184**,   3410-3425   e3417   (2021).
920   https://doi.org:10.1016/j.cell.2021.04.047
921 37 Giraldo, M. I. *et al.* Envelope protein ubiquitination drives entry and pathogenesis of
922   Zika virus. *Nature* **585**, 414-419 (2020). https://doi.org:10.1038/s41586-020-2457-8
923 38 Lu, M. *et al.* E3 ubiquitin ligase tripartite motif 7 positively regulates the TLR4-mediated
924   immune response via its E3 ligase domain in macrophages. *Mol Immunol* **109**, 126-133
925   (2019). https://doi.org:10.1016/j.molimm.2019.01.015
926 39 Stukalov, A. *et al.* Multilevel proteomics reveals host perturbations by SARS-CoV-2 and
927   SARS-CoV. *Nature* **594**, 246-252 (2021). https://doi.org:10.1038/s41586-021-03493-4
928 40 Yuan, Z. *et al.* The E3 Ubiquitin Ligase RNF5 Facilitates SARS-CoV-2 Membrane Protein-
929   Mediated Virion Release. *mBio*, e0316821 (2022). https://doi.org:10.1128/mbio.03168-
930   21
931 41 Zhang, J. *et al.* A systemic and molecular study of subcellular localization of SARS-CoV-2
932   proteins. *Signal Transduct Target Ther* **5**, 269 (2020). https://doi.org:10.1038/s41392-
933   020-00372-8
934 42 Muruato, A. *et al.* Mouse-adapted SARS-CoV-2 protects animals from lethal SARS-CoV
935   challenge. *PLoS Biol* **19**, e3001284 (2021). https://doi.org:10.1371/journal.pbio.3001284
936 43 Bermejo-Jambrina, M. *et al.* Infection and transmission of SARS-CoV-2 depend on
937   heparan   sulfate   proteoglycans.   *EMBO   J*   **40**,   e106765   (2021).
938   https://doi.org:10.15252/embj.2020106765
939 44 Zhang, Q. *et al.* Severe Acute Respiratory Syndrome Coronavirus 2 (SARS-CoV-2)
940   Membrane (M) and Spike (S) Proteins Antagonize Host Type I Interferon Response. *Front*
941   *Cell Infect Microbiol* **11**, 766922 (2021). https://doi.org:10.3389/fcimb.2021.766922
942 45 Chakraborty, A., Diefenbacher, M. E., Mylona, A., Kassel, O. & Behrens, A. The E3
943   ubiquitin ligase Trim7 mediates c-Jun/AP-1 activation by Ras signalling. *Nat Commun* **6**,
944   6782 (2015). https://doi.org:10.1038/ncomms7782
945 46 Li, S. *et al.* SARS-CoV-2 triggers inflammatory responses and cell death through caspase-
946   8   activation.   *Signal   Transduct   Target   Ther*   **5**,   235   (2020).
947   https://doi.org:10.1038/s41392-020-00334-0
948 47 Maharjan, S. *et al.* Apoptosis Enhances the Replication of Human Coronavirus OC43.
949   *Viruses* **13** (2021). https://doi.org:10.3390/v13112199

48   Chen, C. *et al.* CoV-Spectrum: analysis of globally shared SARS-CoV-2 data to identify and characterize new variants. *Bioinformatics* **38**, 1735-1737 (2022). https://doi.org:10.1093/bioinformatics/btab856

49   Danthi, P. Viruses and the Diversity of Cell Death. *Annu Rev Virol* **3**, 533-553 (2016). https://doi.org:10.1146/annurev-virology-110615-042435

50   Barber, G. N. Host defense, viruses and apoptosis. *Cell Death Differ* **8**, 113-126 (2001). https://doi.org:10.1038/sj.cdd.4400823

51   Chu, H. *et al.* Coronaviruses exploit a host cysteine-aspartic protease for replication. *Nature* **609**, 785-792 (2022). https://doi.org:10.1038/s41586-022-05148-4

52   Chu, H. *et al.* Targeting highly pathogenic coronavirus-induced apoptosis reduces viral pathogenesis and disease severity. *Sci Adv* **7** (2021). https://doi.org:10.1126/sciadv.abf8577

53   Diemer, C. *et al.* Cell type-specific cleavage of nucleocapsid protein by effector caspases during SARS coronavirus infection. *J Mol Biol* **376**, 23-34 (2008). https://doi.org:10.1016/j.jmb.2007.11.081

54   Eleouet, J. F. *et al.* The viral nucleocapsid protein of transmissible gastroenteritis coronavirus (TGEV) is cleaved by caspase-6 and -7 during TGEV-induced apoptosis. *J Virol* **74**, 3975-3983 (2000). https://doi.org:10.1128/jvi.74.9.3975-3983.2000

55   Collins, L. T. *et al.* Elucidation of SARS-Cov-2 Budding Mechanisms through Molecular Dynamics Simulations of M and E Protein Complexes. *J Phys Chem Lett* **12**, 12249-12255 (2021). https://doi.org:10.1021/acs.jpclett.1c02955

56   Krieger, E. *et al.* Improving physical realism, stereochemistry, and side-chain accuracy in homology modeling: Four approaches that performed well in CASP8. *Proteins* **77 Suppl 9**, 114-122 (2009). https://doi.org:10.1002/prot.22570

57   Teruel, N., Borges, V. M. & Najmanovich, R. Surfaces: a software to quantify and visualize interactions within and between proteins and ligands. *Bioinformatics* **39** (2023). https://doi.org:10.1093/bioinformatics/btad608

58   Hsu, R. J. *et al.* The Role of Cytokines and Chemokines in Severe Acute Respiratory Syndrome Coronavirus 2 Infections. *Front Immunol* **13**, 832394 (2022). https://doi.org:10.3389/fimmu.2022.832394

59   Huang, C. *et al.* Clinical features of patients infected with 2019 novel coronavirus in Wuhan, China. *Lancet* **395**, 497-506 (2020). https://doi.org:10.1016/S0140-6736(20)30183-5

60   Schett, G., Sticherling, M. & Neurath, M. F. COVID-19: risk for cytokine targeting in chronic inflammatory diseases? *Nat Rev Immunol* **20**, 271-272 (2020). https://doi.org:10.1038/s41577-020-0312-7

61   Chen, G. *et al.* Clinical and immunological features of severe and moderate coronavirus disease 2019. *J Clin Invest* **130**, 2620-2629 (2020). https://doi.org:10.1172/JCI137244

62   Tay, M. Z., Poh, C. M., Renia, L., MacAry, P. A. & Ng, L. F. P. The trinity of COVID-19: immunity, inflammation and intervention. *Nat Rev Immunol* **20**, 363-374 (2020). https://doi.org:10.1038/s41577-020-0311-8

63   Wong, R. S. Y. Inflammation in COVID-19: from pathogenesis to treatment. *Int J Clin Exp Pathol* **14**, 831-844 (2021).

22

993 64 Vanderheiden, A. *et al.* CCR2 Signaling Restricts SARS-CoV-2 Infection. *mBio* **12**,
994   e0274921 (2021). https://doi.org/10.1128/mBio.02749-21

995 65 Zhou, Y. *et al.* Pathogenic T-cells and inflammatory monocytes incite inflammatory
996   storms in severe COVID-19 patients. *Natl Sci Rev* **7**, 998-1002 (2020).
997   https://doi.org/10.1093/nsr/nwaa041

998 66 Chevrier, S. *et al.* A distinct innate immune signature marks progression from mild to
999   severe COVID-19. *Cell Rep Med* **2**, 100166 (2021).
1000   https://doi.org/10.1016/j.xcrm.2020.100166

1001 67 Veras, F. P. *et al.* SARS-CoV-2-triggered neutrophil extracellular traps mediate COVID-19
1002   pathology. *J Exp Med* **217** (2020). https://doi.org/10.1084/jem.20201129

1003 68 Ardi, V. C., Kupriyanova, T. A., Deryugina, E. I. & Quigley, J. P. Human neutrophils
1004   uniquely release TIMP-free MMP-9 to provide a potent catalytic stimulator of
1005   angiogenesis. *Proc Natl Acad Sci U S A* **104**, 20262-20267 (2007).
1006   https://doi.org/10.1073/pnas.0706438104

1007 69 Christoffersson, G. *et al.* Clinical and experimental pancreatic islet transplantation to
1008   striated muscle: establishment of a vascular system similar to that in native islets.
1009   *Diabetes* **59**, 2569-2578 (2010). https://doi.org/10.2337/db10-0205

1010 70 Nishio, N., Okawa, Y., Sakurai, H. & Isobe, K. Neutrophil depletion delays wound repair in
1011   aged mice. *Age (Dordr)* **30**, 11-19 (2008). https://doi.org/10.1007/s11357-007-9043-y

1012 71 Hingorani, D. V. *et al.* Impact of MMP-2 and MMP-9 enzyme activity on wound healing,
1013   tumor growth and RACPP cleavage. *PLoS One* **13**, e0198464 (2018).
1014   https://doi.org/10.1371/journal.pone.0198464

1015 72 Mohan, R. *et al.* Matrix metalloproteinase gelatinase B (MMP-9) coordinates and effects
1016   epithelial regeneration. *J Biol Chem* **277**, 2065-2072 (2002).
1017   https://doi.org/10.1074/jbc.M107611200

1018 73 Vrints, C. J. M. *et al.* Endothelialitis plays a central role in the pathophysiology of severe
1019   COVID-19 and its cardiovascular complications. *Acta Cardiol* **76**, 109-124 (2021).
1020   https://doi.org/10.1080/00015385.2020.1846921

1021 74 Yang, B. *et al.* Negative Regulation of RNF90 on RNA Virus-Triggered Antiviral Immune
1022   Responses Targeting MAVS. *Front Immunol* **12**, 730483 (2021).
1023   https://doi.org/10.3389/fimmu.2021.730483

1024 75 Lokugamage, K. G. *et al.* Type I Interferon Susceptibility Distinguishes SARS-CoV-2 from
1025   SARS-CoV. *J Virol* **94** (2020). https://doi.org/10.1128/JVI.01410-20

1026 76 Oguntuyo, K. Y. *et al.* Quantifying Absolute Neutralization Titers against SARS-CoV-2 by a
1027   Standardized Virus Neutralization Assay Allows for Cross-Cohort Comparisons of COVID-
1028   19 Sera. *mBio* **12** (2021). https://doi.org/10.1128/mBio.02492-20

1029 77 Xie, X. *et al.* Engineering SARS-CoV-2 using a reverse genetic system. *Nat Protoc* **16**,
1030   1761-1784 (2021). https://doi.org/10.1038/s41596-021-00491-8

1031 78 Xie, X. *et al.* An Infectious cDNA Clone of SARS-CoV-2. *Cell Host Microbe* **27**, 841-848
1032   e843 (2020). https://doi.org/10.1016/j.chom.2020.04.004

1033 79 Rajsbaum, R. *et al.* Unanchored K48-linked polyubiquitin synthesized by the E3-ubiquitin
1034   ligase TRIM6 stimulates the interferon-IKKepsilon kinase-mediated antiviral response.
1035   *Immunity* **40**, 880-895 (2014). https://doi.org/10.1016/j.immuni.2014.04.018

1036 80 Hadjadj, J. *et al.* Impaired type I interferon activity and inflammatory responses in
1037   severe COVID-19 patients. *Science* **369**, 718-724 (2020).
1038   https://doi.org:10.1126/science.abc6027
1039 81 Xu, R., Shi, M., Li, J., Song, P. & Li, N. Construction of SARS-CoV-2 Virus-Like Particles by
1040   Mammalian Expression System. *Front Bioeng Biotechnol* **8**, 862 (2020).
1041   https://doi.org:10.3389/fbioe.2020.00862
1042 82 Garcia, M. *et al.* Innate lymphoid cell composition associates with COVID-19 disease
1043   severity. *Clin Transl Immunology* **9**, e1224 (2020). https://doi.org:10.1002/cti2.1224
1044 83 Klopfleisch, R. Multiparametric and semiquantitative scoring systems for the evaluation
1045   of mouse model histopathology--a systematic review. *BMC Vet Res* **9**, 123 (2013).
1046   https://doi.org:10.1186/1746-6148-9-123
1047 84 Ivan Aksamentov, C. R., Emma B. Hodcroft, and & Neher, R. A. Nextclade: clade
1048   assignment, mutation calling and quality control for viral genomes. *Journal of Open*
1049   *Source Software* **6** (2021). https://doi.org: https://doi.org/10.21105/joss.03773
1050 85 Jo, S., Kim, T., Iyer, V. G. & Im, W. CHARMM-GUI: a web-based graphical user interface
1051   for CHARMM. *J Comput Chem* **29**, 1859-1865 (2008). https://doi.org:10.1002/jcc.20945
1052 86 Lee, J. *et al.* CHARMM-GUI Membrane Builder for Complex Biological Membrane
1053   Simulations with Glycolipids and Lipoglycans. *J Chem Theory Comput* **15**, 775-786 (2019).
1054   https://doi.org:10.1021/acs.jctc.8b01066
1055 87 Wu, E. L. *et al.* CHARMM-GUI Membrane Builder toward realistic biological membrane
1056   simulations. *J Comput Chem* **35**, 1997-2004 (2014). https://doi.org:10.1002/jcc.23702

1057
1058
1059
1060
1061
1062
1063
1064
1065
1066
1067
1068
1069
1070
1071
1072
1073
1074
1075
1076
1077
1078
1079
1080

24

1081 **FIGURES**

1082
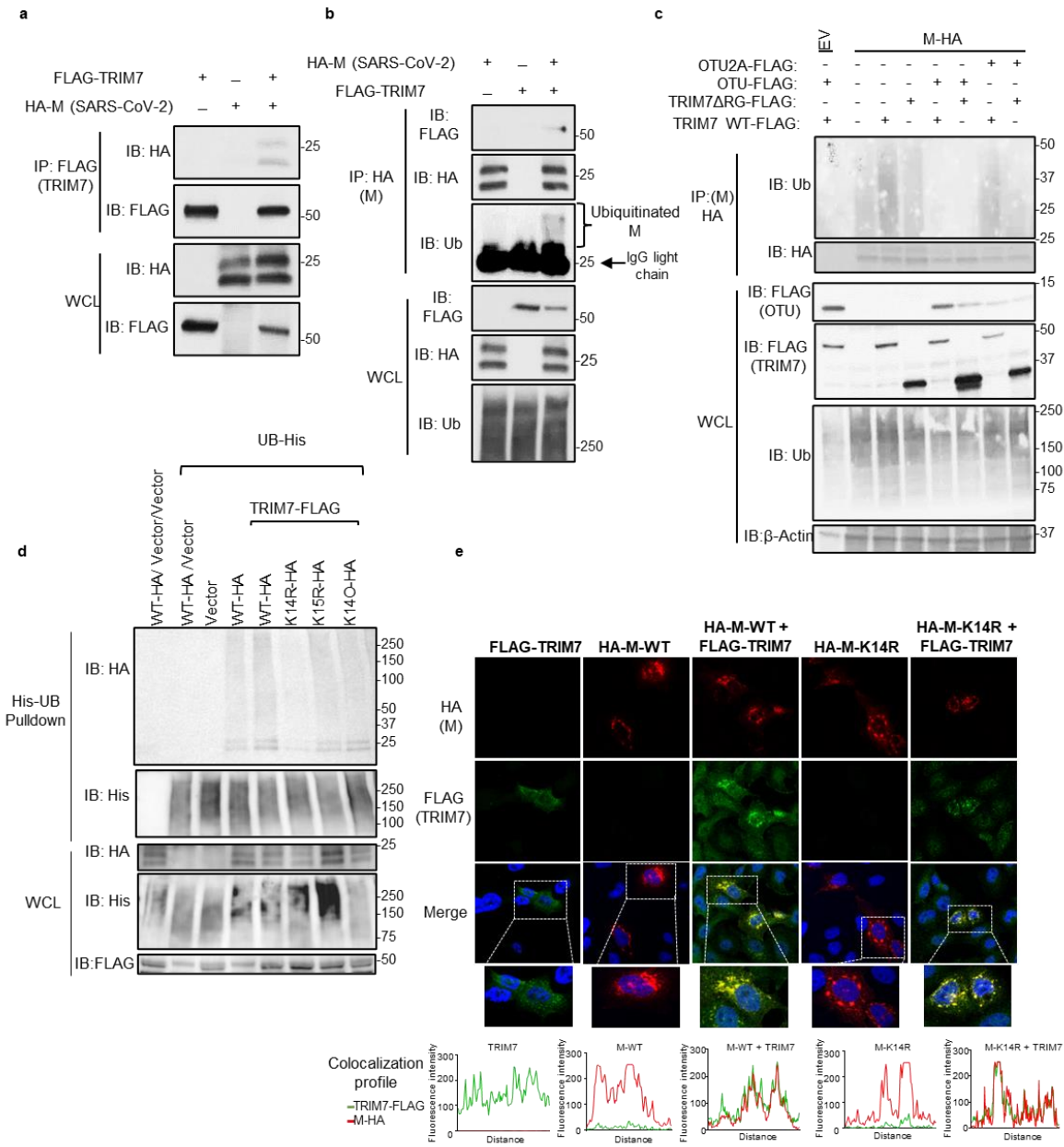
1083
1084
1085
1086
1087
1088
1089
1090
1091
1092

25

1093 **Figure 1. TRIM7 ubiquitinates SARS-CoV-2 Membrane protein**. a-b) HEK 293T cells
1094 were transfected with Vector, M-HA, +/- TRIM7 WT-FLAG, and immunoprecipitated
1095 using anti-FLAG beads (a) or anti-HA beads (b). c) HEK293T cells transfected with M-
1096 HA, TRIM7 WT-FLAG or TRIM7-ΔRING-FLAG +/- OTU-WT-FLAG or OTU-2A-FLAG
1097 followed by immunoprecipitation with anti-HA beads, d) denaturing pulldown using
1098 NiNTA beads. HEK293T cells transfected with His-Ub, M WT-HA, M-K14R, M-K15R, M-
1099 K14O (all Ks mutated to Rs except for K14), +/- TRIM7 WT-FLAG. e) Confocal
1100 microscopy of Hela cells transfected with TRIM7-FLAG (488), M WT-HA or M K14R-HA
1101 (555), for 24 hours. Colocalization profile graphs are shown.
1102
1103
1104
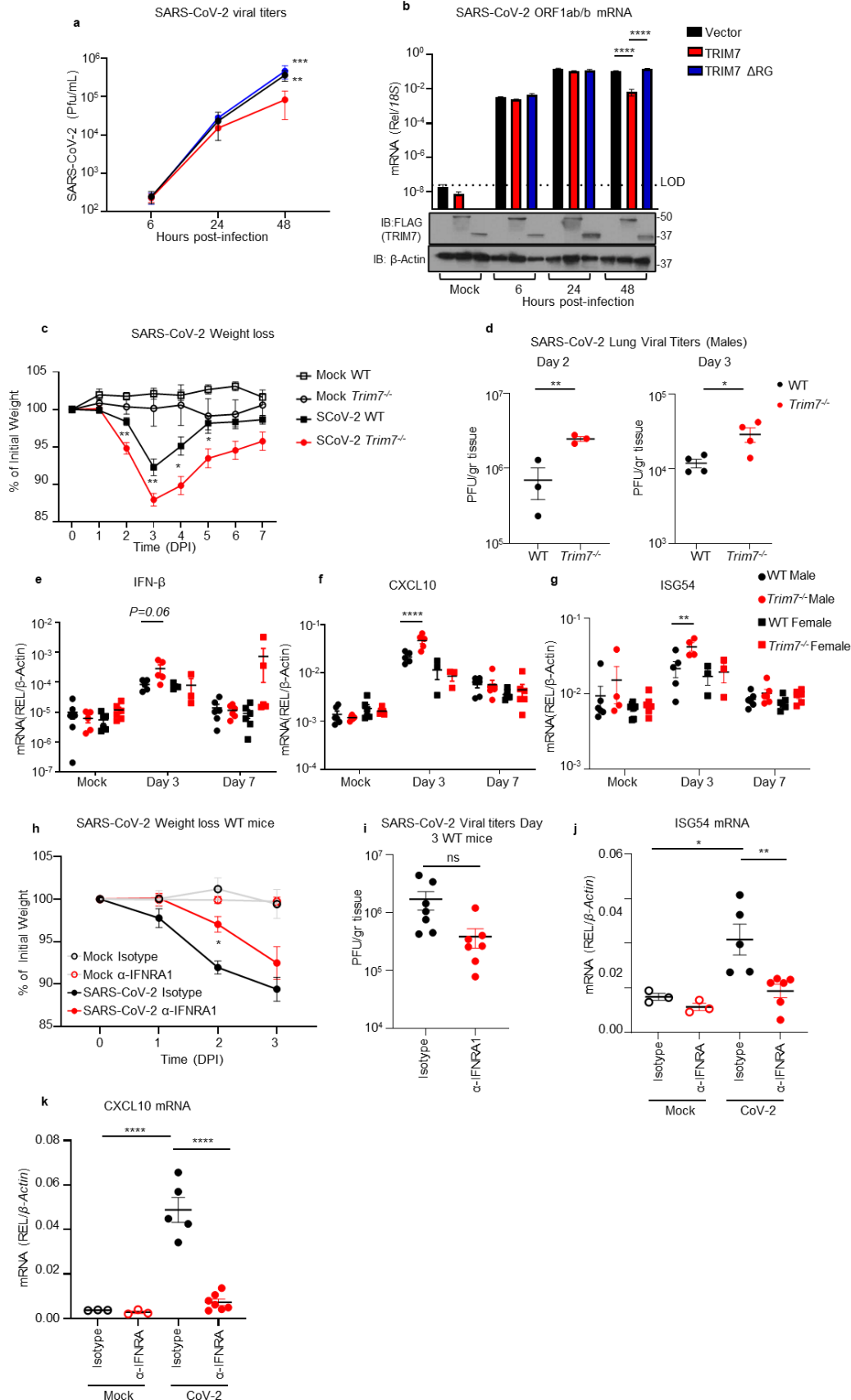
26

Figure 2. TRIM7 has antiviral activity during SARS-CoV-2 infection. a-b) HEK293T-hACE-2 cells were transfected with TRIM7 WT or TRIM7-ΔRING followed by infected with SARS-CoV-2 (MOI 0.1). Viral titers quantified by plaque assay (a) or viral RNA by qPCR (b). Bottom panel in b shows Immunoblot control for TRIM7 expression. c-g) C57BL/6NJ WT (n=18 9 females, 9 males) and *Trim7*^{-/-} mice (n=23 10 females, 13 males) infected with maSARS-CoV-2 ($1x10^6$ PFU). Weight loss (c), viral titers by plaque assay (d), gene expression in lung tissue by qPCR (e: IFN-β, f: CXCL10, g: ISG54). h-j) IFNAR1 blockade: C57BL/6J WT (n=7/group 5 females and 2 males) were treated with anti-IFNRA1 or isotype 24h before infection with maSARS-CoV-2 ($1x10^6$ PFU). Weight loss (h), lung viral titers (i) and gene expression by qPCR of ISG54 (j) CXCL10 (k). Data are depicted as Mean + SEM. (a-b) are representative of 3 independent experiments in triplicates 2-way ANOVA Tukey's multiple comparisons. (c) is combined data from 3 independent experiments 2-way ANOVA Tukey's multiple comparisons. (d-g) representative data of 3 independent experiments (d) T-test. (e-g) 2-way ANOVA Tukey's multiple comparisons. (h) representative data 2-way ANOVA Tukey's multiple comparisons. (i) T-test analysis. (j-k) representative data one-way ANOVA Tukey's multiple comparisons. $p < 0.001$ **, $p < 0.0001$ ***, $p < 0.00001$ ****.

28

1152

29
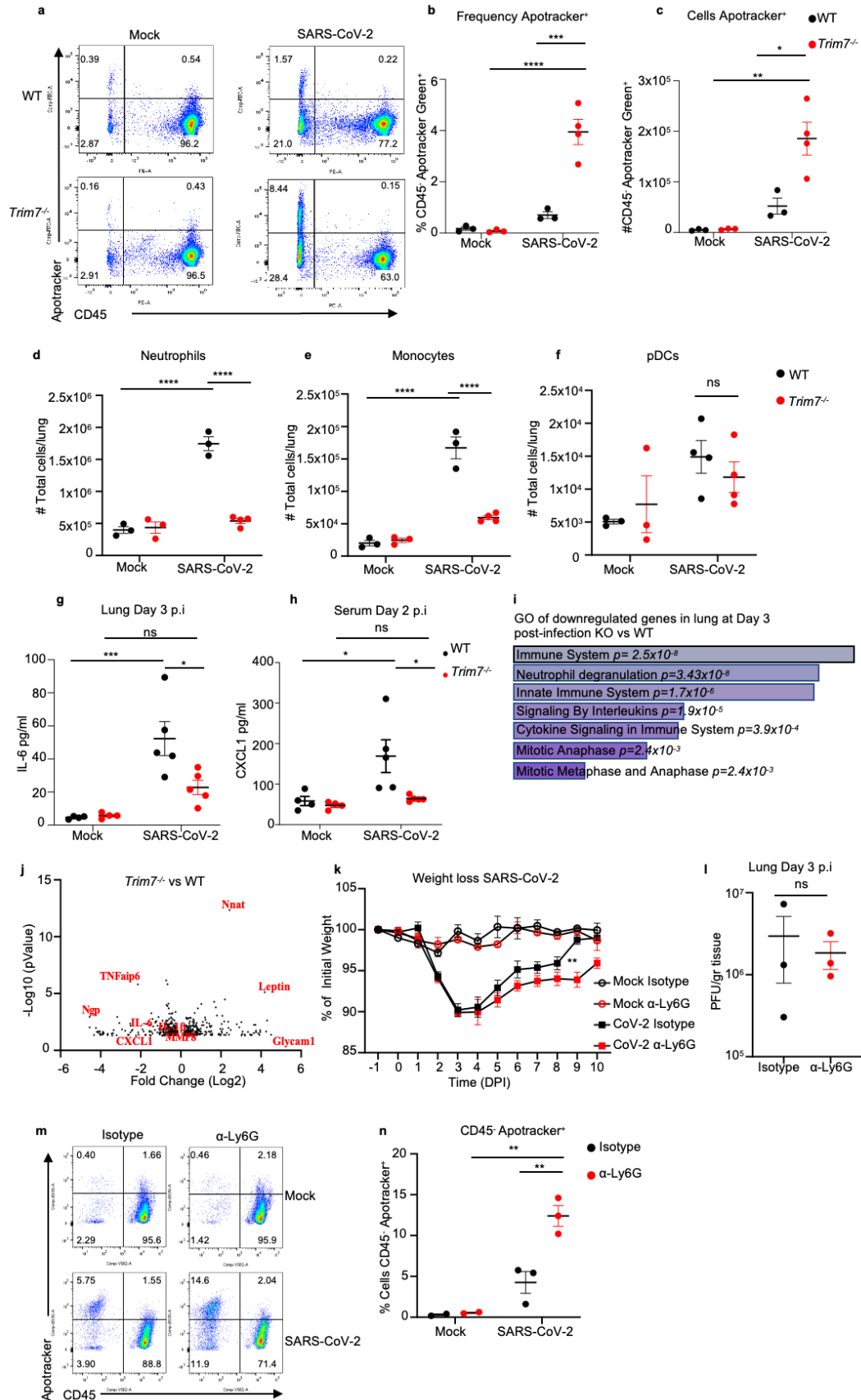
Figure 3. *Trim7 $^{-/-}$* mice have impaired innate immune response to SARS-CoV-2 infection. Male C57BL/6NJ WT and *Trim7$^{-/-}$* mice were infected with maSARS-CoV-2 (WT n=3, KO n=4). At day 3 post-infection lung cells were stained for CD45 and Apotracker Green and a representative FACS dot plot shown in (a), frequency of CD45-Apotracker Green$^+$ cells (b), or total number of cells per lung (c), total number of neutrophils CD45$^+$CD11c$^-$CD11b$^+$Ly6C^{int}Ly6G^{hi} (d), monocytes CD45$^+$CD11c$^-$CD11b$^+$Ly6C^{hi}Ly6G$^-$ (e), pDCs CD45$^+$CD11c^{lo}PDCA-1$^+$CD11b$^-$ (f). 23-Bioplex analysis from lung (g) or serum (h). IL-6 and CXCL1 are shown. i) Gene ontology graph of genes downregulated in the lung of *Trim7$^{-/-}$* mice at day 3 post-infection. j) Volcano plot of genes changing in lung in WT and *Trim7$^{-/-}$* mice at day 3 post-infection. k) Weight loss graph of WT mice depleted of neutrophils using anti Ly6G antibody or isotype as control infected with maSARS-CoV-2 (n=8). l) viral titers in the lung of mice infected as (k) (n=3), (m) representative dot blot of lung cells stained using CD45 and Apotracker Green, (n) Frequency of cells CD45- Apotracker Green$^+$. Data are depicted as Mean ± SEM. (b-h) and (k), representative data of at least 2 independent experiments 2-way ANOVA Tukey's multiple comparisons. (l), T-test analysis. (n), 2-way ANOVA Tukey's multiple comparisons. $p < 0.001$ **, $p < 0.0001$ ***, $p < 0.00001$ ****.
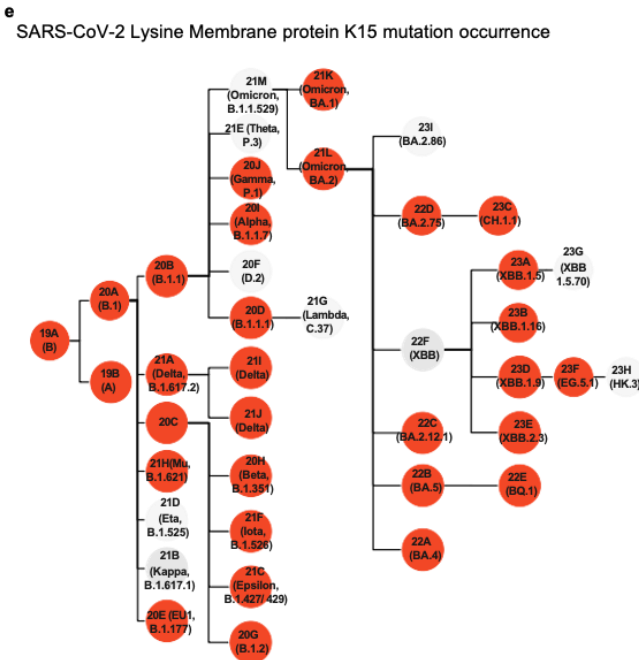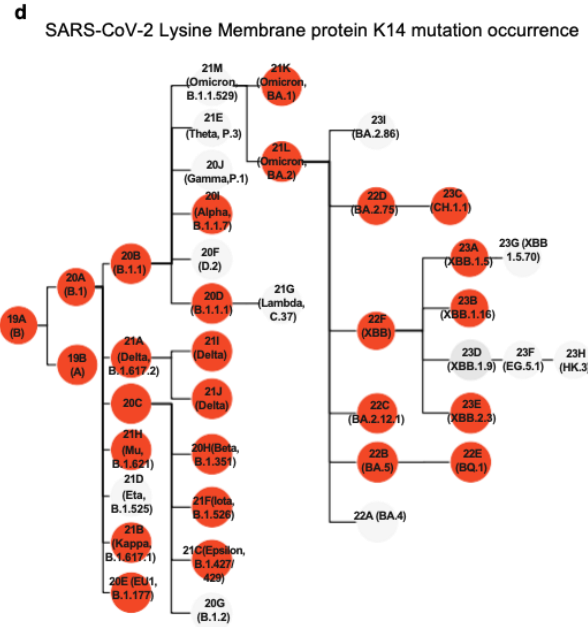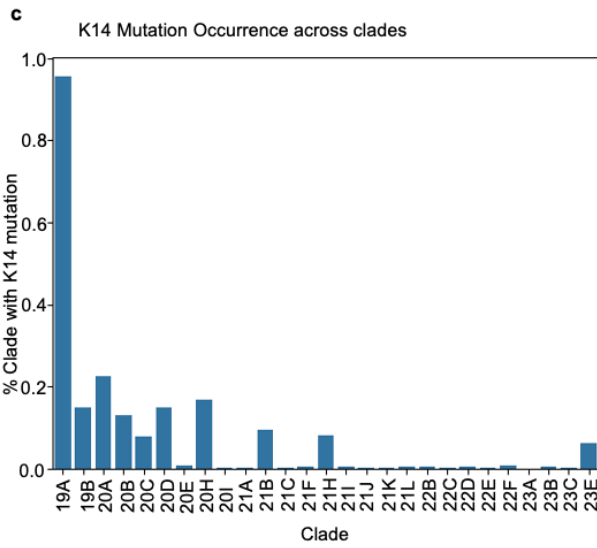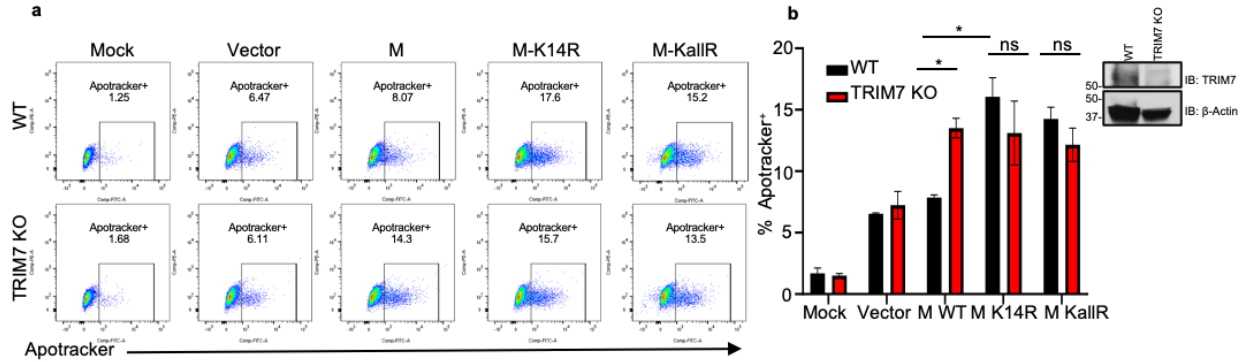
Figure 4. Mutations on M lysine 14 induce apoptosis and are present in circulating stains of SARS-CoV-2. a-b) A549 WT or TRIM7 KO transfected with M-WT, M-K14R, or M-KallR mutants for 24h and then stained with Apotracker Green, representative dot blot (a), frequency of cells Apotracker+ (b). c-d) M lysine mutations in SARS-CoV-2 sequences. c) percentage of occurrence of M-K14 mutation across the clades. d) membrane protein K14 mutation occurrence. e) membrane protein K15 mutation occurrence. Red highlighted nodes indicate at least one mutation occurrence in the specific clade. Data are depicted as Mean ± SEM. b, representative data of 2 independent experiments in duplicates 2-way ANOVA Tukey's multiple comparisons test. $p < 0.001$ **, $p < 0.0001$ ***, $p < 0.00001$ ****.

1247
1248
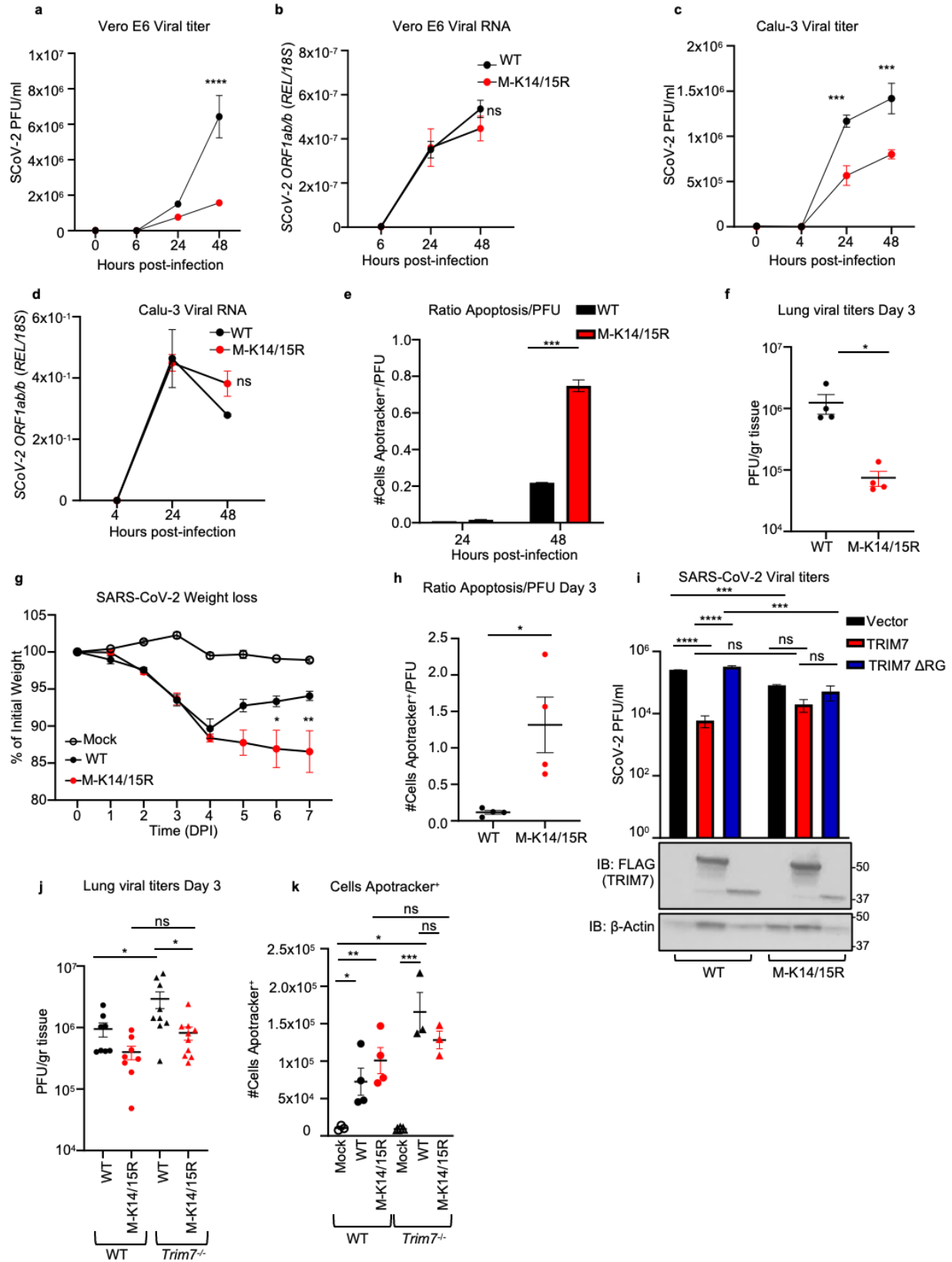
Figure 5. Recombinant virus with M K14/K15 mutations shows increased pathogenesis. Vero E6 or Calu-3 infected with SARS-Cov-2 WT or M-K14/15R MOI 0.1 and 1 respectively. a) viral titers and b) viral RNA in Vero E6. c) viral titers and d, viral RNA in Calu-3. e) ratio of cells in apoptosis Apotracker$^+$ normalized by viral titers (Apotracker$^+$/PFU) in Calu-3 cells. WT C57BL/6J male mice infected with SARS-CoV-2 WT (n=8) or M-K14/15R mutant viruses (n=10) and mock (n=5). At day 3 post-infection 4 mice were euthanized and lung collected for plaque assay and flow cytometry. f) viral titers in lung. g) weight loss curve. h) ratio of cells in apoptosis in lung (Apotracker$^+$/PFU). i) viral titers of HEK 293T-hACE-2 cells transfected with TRIM7 WT or TRIM7ΔRING and infected with SARS-CoV-2 WT or MK14/15R at MOI 0.1 (bottom panel western blot analysis of overexpression of TRIM7). WT (n=8, 6 males, 2 females) and *Trim7$^{-/-}$* (n=9 and 11, 7 or 9 males and 2 females) mice infected intranasal with SARS-CoV-2 WT or M-K14/15R and euthanized at day 3 post-infection. j) lung viral titers. k) total number of cells in apoptosis (CD45 $^+$Apotracker$^+$). Data are depicted as Mean ± SEM. a-e) are representative of 3 independent experiments in triplicate 2-way ANOVA Tukey's multiple comparisons. f-h) is presentative data of at least 2 independent experiments. f) and h) t-test analysis. g) 2-way ANOVA Tukey's multiple comparisons. i) is presentative data of at least 3 independent experiments in triplicates, 2-way ANOVA Tukey's multiple comparisons. j) is combined data of 2 independent experiments, k) is representative data of 1 of the 2 independent experiments of j) one-way ANOVA Tukey's multiple comparisons. $p < 0.001$ **, $p < 0.0001$ ***, $p < 0.00001$ ****.

1295
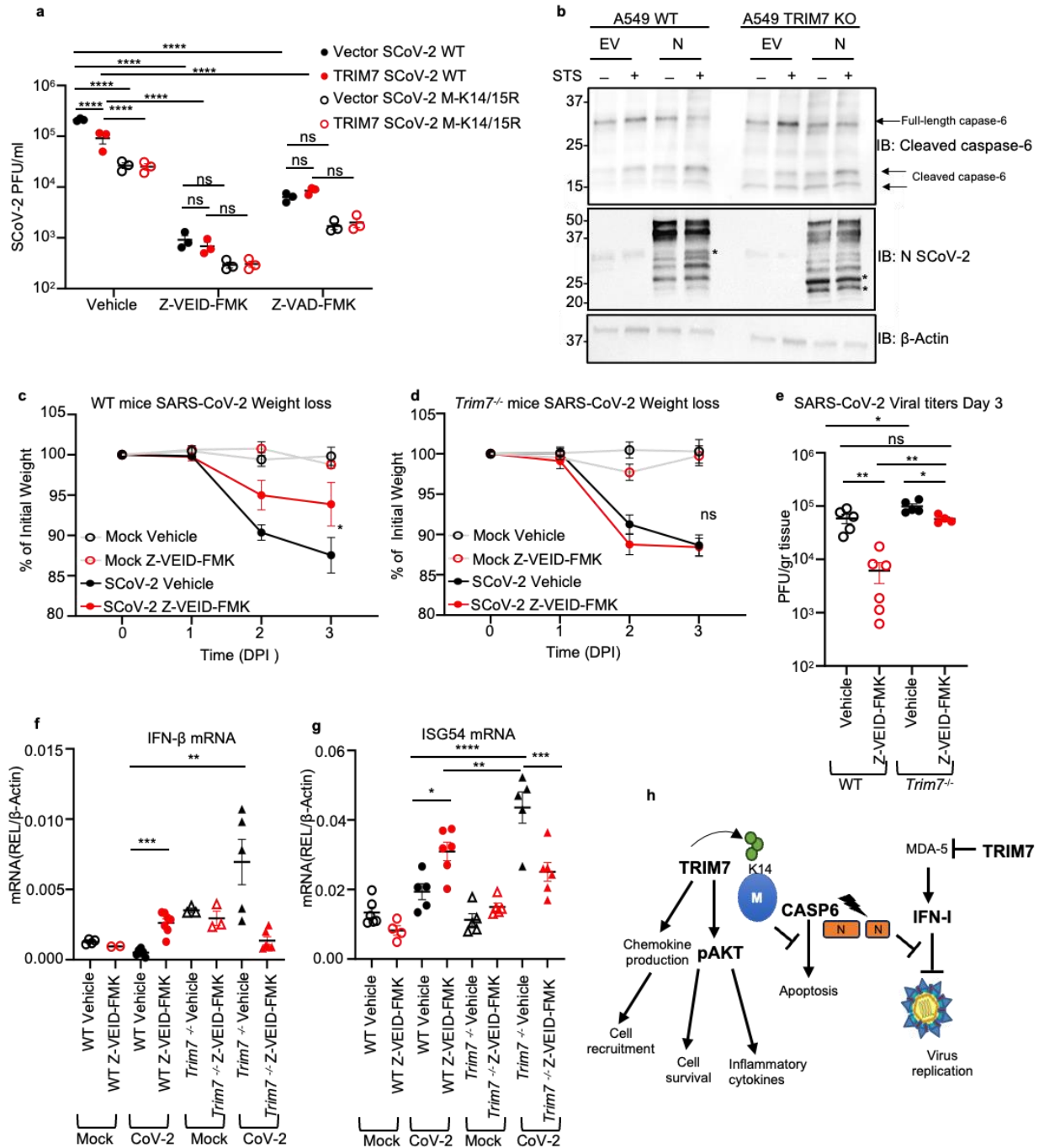
1296
1297
1298
1299
1300
1301
1302
1303
1304

1305
1306 **Figure 6. TRIM7 mediates its antiviral effects by inhibiting caspase-6 activation**. a)
1307 viral titers of HEK 293T-hACE-2 cells overexpressing TRIM7 WT and infected with
1308 SARS-CoV-2 WT or M-K14/15R at MOI 0.1 and treated with vehicle (DMSO) or 50µM of
1309 Z-VEID-FMK 24h post-infection. b) western blot analysis of A549 WT and TRIM7KO
1310 cells transfected with SARS-CoV-2 N protein or empty vector and treated with
1311 Staurosporine (STS) *indicates cleaved form of N. c) weight loss of WT female mice
1312 infected intranasal with SARS-CoV-2 WT treated intraperitoneal with caspase-6 inhibitor
1313 or vehicle and lung collected at day 3 post-infection. mocks (n=6 each) vehicle (n=5) or
1314 Z-VEID-FMK (n=6) d) weight loss $Trim7^{-/-}$ female mice as in (c) vehicle mocks (n=5
1315 each) infected vehicle (n=4) or Z-VEID-FMK (n=6). e) lung viral titers. f) IFN-β mRNA
1316 and (g) ISG54mRNA expression levels in lung. h) scheme of the multiple functions of
1317 TRIM7 during SARS-CoV-2 infection. Data are depicted as Mean ± SEM. a) is
1318 presentative data of at least 2 independent experiments in triplicates, 2-way ANOVA
1319 Tukey's multiple comparisons. c-d) are representative data of 2 independent
1320 experiments 2-way ANOVA Tukey's multiple comparisons and e-f) one-way ANOVA
1321 Tukey's multiple comparisons. $p < 0.001$ **, $p < 0.0001$ ***, $p < 0.00001$ ****.
1322
1323

36